Radio Frequency Power Combining With Reactance Steering Network for Fusion Plasma Heating

Tanuj Sen, *Student Member, IEEE*, Mian Liao, *Student Member, IEEE*, Youssef Elasser, *Student Member, IEEE*, and Minjie Chen, *Senior Member, IEEE*

***Abstract*—This article presents the design and implementation of an amplitude modulated radio-frequency (RF) power combiner system using a reactance steering network for driving variable impedance Inductively Coupled Plasma (ICP) heating coils in fusion reactors. The variation in the impedance of ICP coils depends greatly on factors such as the plasma electron density, pressure or temperature of the plasma. The matching network is used to reduce the range of variation in the ICP impedance, while the reactance steering network functions to make the branch impedances almost completely resistive. A prototype is designed, with two equivalent resonant Class-E power amplifiers, connected in parallel through a dedicated reactance steering network to a matching network, which in turn is connected to a load that emulates the impedance characteristics of an ICP coil. The frequency of system operation is set as 10 MHz, capable of driving the ICP load with 225 W of power at a peak efficiency of 75.6% in continuous operation mode. The simulation and experimental results, collected for a range of load points, both highlight the effectiveness of the combined reactance steering network and matching network structure when powering variable impedance ICP coils using impedance sensitive resonant power amplifiers, operating with ZVS.**

***Index Terms*—Class-E, electron density, fusion power generation, ICP coil, plasma, reactance steering network (RSN), resonant power amplifier, zero voltage switching (ZVS).**

I. Introduction

FUSION energy is gradually becoming one of the leading candidates as a clean alternate energy source for the future, among a vast array of other renewable sources, because of its immense potential. Energy from fusion is extracted from fusion reactions, wherein two nuclei of a lighter element like Hydrogen collide and fuse into a heavier element, such as Helium, while releasing energy as a by-product. However, the challenge associated with such energy generation is that these reactions can only take place under extreme temperatures and pressures, similar to the conditions found inside the cores of stars. In order to replicate such reactions on earth, a dedicated fusion reaction chamber is required, which holds plasma at incredibly high temperatures [2]. This superheated plasma acts as the fuel necessary for igniting fusion reactions. Magnetic confinement using strong magnetic fields is used to confine the plasma inside the vacuumized fusion reactor chambers. A schematic representation of the tokamak fusion reactor proposed and being developed by International Thermonuclear Experimental Reactor (ITER) is shown in Fig. 1.

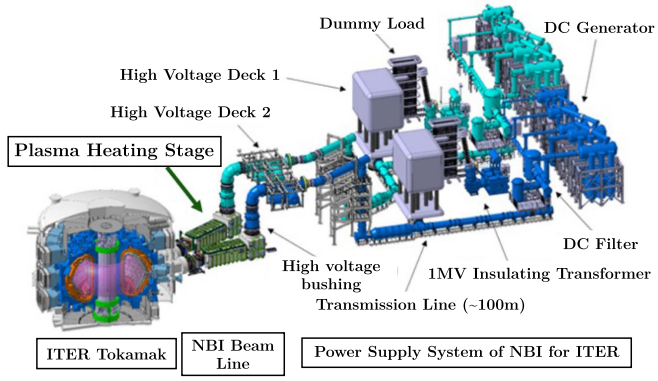

Fig. 1. Illustration of the fusion reactor system proposed and being developed by ITER. The size of the Neutral Beam Injector (NBI), which injects fuel for fusion into the reactor, and its power supply system is much larger than that of the reactor itself. Source of the original picture is [3].

Given the requirement of superheated plasma as fuel for fusion reactors, one of the challenges associated with fusion energy generation is the creation of such a plasma medium. Since plasma for fusion reactors needs to be heated to extreme temperatures [4], power in excess of millions of watts is required to be delivered to the plasma as a high frequency ac source [5], [6]. This is where switched-mode power electronic converters using semiconductor devices can find application as power sources for heating plasma. RF sources can be designed using semiconductor devices based off of Silicon Carbide (SiC) or Gallium Nitride (GaN), which can produce RF waves to transfer power to the plasma. However, given the need for high power for heating plasma for fusion reactors, these switches are required to handle large currents at high-frequency (HF) or very-high-frequency (VHF) switching frequency. This is where the current technology of semiconductor devices reach their limits, as shown in Fig. 2. SiC devices are capable of handling high power applications but are limited in their frequency of

Received 5 October 2024; revised 31 January 2025 and 6 May 2025; accepted 24 June 2025. Date of publication 30 June 2025; date of current version 5 August 2025. This work was supported by the US DOE ARPA-E GAMOW Program. An earlier version of this paper was presented in part at the 2024 IEEE Applied Power Electronics Conference and Exposition (APEC) [DOI: 10.1109/APEC48139.2024.10509276]. Recommended for publication by Associate Editor C. Fernandez. *(Corresponding Author: Minjie Chen.)*

The authors are with the Department of Electrical and Computer Engineering and Andlinger Center for Energy and the Environment, Princeton University, Princeton, NJ 08540 USA (e-mail: minjie@princeton.edu).

Color versions of one or more figures in this article are available at https://doi.org/10.1109/TPEL.2025.3584308.

Digital Object Identifier 10.1109/TPEL.2025.3584308

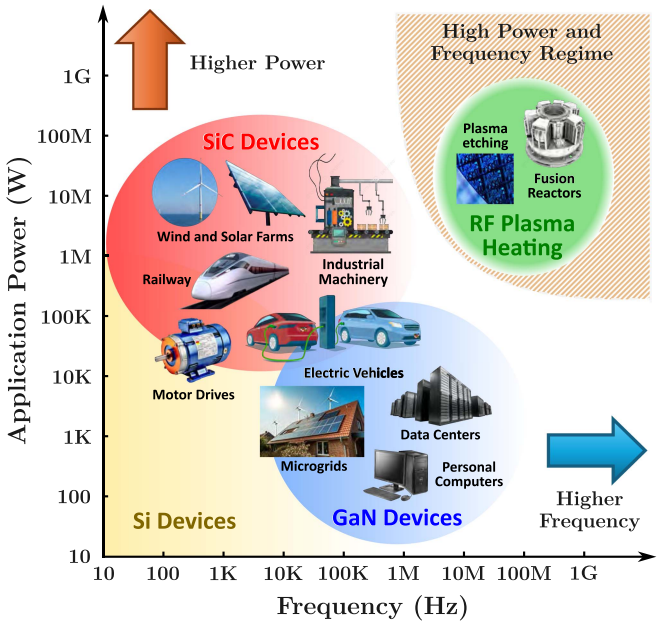

Fig. 2. Power and frequency application ranges for SiC and GaN-based semiconductor switching devices [7], [8] in comparison to the power and frequency requirements of RF sources used for plasma heating [4], [5], [6].

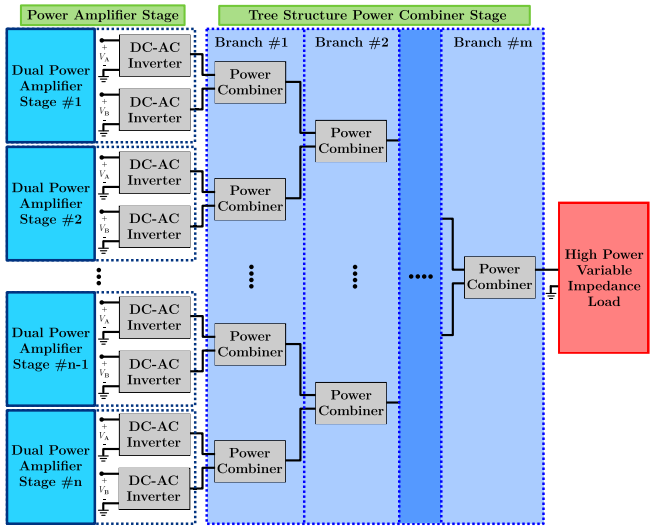

Fig. 3. Proposed tree structure configuration for a high-power and high-frequency RF source for plasma heating applications using power combiners.

operation, whereas GaN based devices are capable of achieving faster switching speeds, but are limited in their power handling capacity [7], [8]. This is a key challenge of employing state-of-the-art power semiconductor devices for designing power electronics for fusion reactors.

Conventional power semiconductor device based power sources for HF and VHF applications involve linear power amplifiers, such as the Class A and Class B amplifiers. However, because of their low operational efficiency, focus has shifted to the use of switched-mode high-frequency resonant power amplifiers, which make use of semiconductor devices. These power amplifiers, such as the Class-E [9] and the Class-Φ_2[10], have better efficiency due to zero-voltage-switching (ZVS). However, the performance of such amplifiers is susceptible to variable load impedance. The design of such power amplifiers is usually optimized around a fixed output load and frequency. Since the plasma impedance varies greatly with respect to its composition, electron density, collision frequency, temperature etc., plasma itself falls into the class of variable impedances. As a result, for plasma heating applications for fusion, design of switched-mode resonant power sources require the consideration of two main constraints: (1) providing high power at high frequency and (2) being able to handle variable output impedances. One solution for such constraints is to design several equivalent lower power high-frequency resonant power amplifiers, which can be tied together in parallel, using power combiners. The main functions of the power combiner circuit would be aggregate power from numerous small scale power sources and deliver the required amount of power for plasma heating, as well as to reduce the impedance variation seen at the output terminals of the resonant power amplifiers [11]. A conceptual representation of the proposed high-power high-frequency switched-mode resonant power architecture is shown in Fig. 3.

Previous research works have made significant forays to make the operation of high-frequency switched-mode resonant power amplifiers more robust, so that they are able to handle variable load impedances [12]. The design of switch-mode amplifiers which are independent of load variations was presented in [13], and in [14], [15], [16], and [17] with various power combiner networks. Tunable Matching Networks (TMNs) [18], [19], [20] have also been used previously to significantly reduce variations in the output load impedance. Such an approach involves the use of capacitor and/or inductor banks, and actively switching between different combinations of such passive components, for properly matching the designed power amplifier to the output load value. TMNs have also been used for making power amplifiers capable of driving variable impedance inductively coupled plasma (ICP) loads, as in [21], where the authors present an implementation of the TMN with phase-switch impedance modulation (PSIM). The resistance compression network (RCN) presented in [11], is used in conjunction with an impedance transformation network in [22], enabling switched-mode power amplifiers to drive ICPs. Other works involve the reactance compensation technique [23] and reactance compensation coupled with frequency selection networks [24] to create wideband switched-mode power amplifiers for driving variable loads.

This article presents the principles and practical implementation of a radio frequency power combining system with reactance steering network for fusion plasma heating. The key contributions of this article are as follows:

1) Motivated the use of distributed power conversion for plasma heating applications in fusion energy systems in Section I.
2) Physics-based modeling of the plasma load for fusion reaction, elaborated in Sections II and III.
3) The design consideration for a low power ICP design driven by two switch-mode power amplifiers, an RSN, and a matching network, as discussed in Section IV.

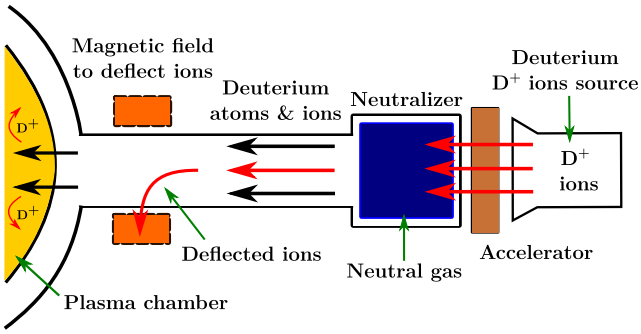

Fig. 4. Representative diagram of the working principle of a neutral beam injector for heating plasma. Picture taken and modified from [25].

4) Section V presents a prototype implementing this design, operating two equivalent Class E inverters at 10 MHz with 200 W and 75% dc–dc efficiency.

The analysis, simulation, and experimental results verify the effectiveness of the proposed technique in driving variable impedance inductively coupled plasma loads.

II. Plasma Heating in Fusion Reactors

Plasma heating for fusion reactors is usually achieved by two main heating techniques [25], [26]. One of the techniques is known as neutral beam heating, where beams of neutral deuterium atoms are injected into the plasma inside the reactor chamber. Inside the plasma, these beams get ionized and get trapped by the magnetic fields of the chamber. These highly energetic ionized beams then heat up the plasma through collisions. The operating principle of neutral beam heating is shown in Fig. 4. This plasma heating method is currently being adopted by ITER for their experimental fusion reactor, as shown in Fig. 1. The other widely used method for heating up and igniting the plasma is through radio frequency (RF) heating. The plasma absorbs power when the frequency of the RF waves is tuned to the resonance frequency of the ions or electrons in the plasma, which in turn heats the plasma. These high-power RF waves are usually produced by using gyrotrons [26], by accelerating electron beams through strong electromagnetic fields generated by superconducting magnetic coils, as shown in Fig. 5. Both these techniques require power in excess of millions of watts, for heating the plasma to the required temperatures for fusion reactions to take place. The working mechanism and structure of these plasma heating apparatuses are quite complicated and bulky, requiring the constant monitoring of several physical parameters to ensure consistent operation. Moreover, their maintenance is also quite difficult, expensive, and time consuming [27]. The use of microwaves for heating plasma is also being investigated [28], as this would allow the size of the fusion chambers to be considerably minimized.

Another way of heating plasma, with considerably simpler construction, is by means of an RF antenna that is inductively coupled to the plasma contained inside a vacuum chamber. Such RF antenna, capable of producing high-power RF waves, are designed either as a planar coil, which is placed on top of the

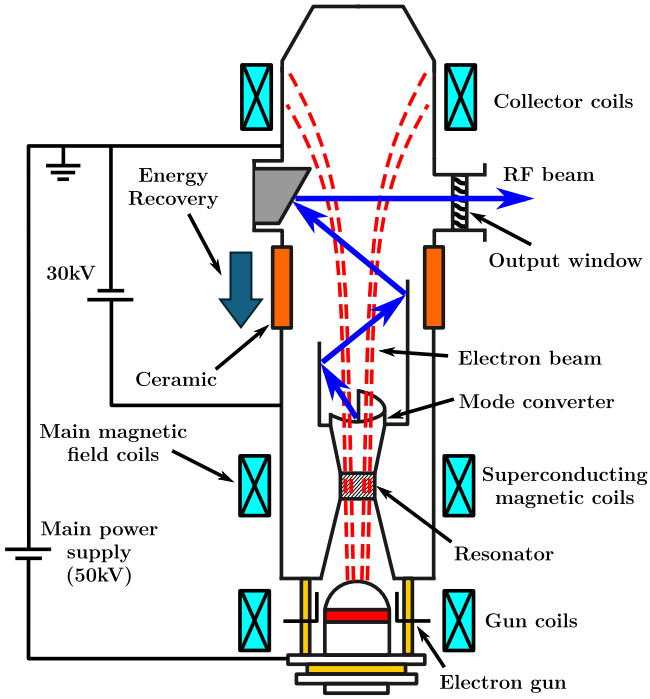

Fig. 5. Schematic diagram showing the construction and working of a gyrotron generating high power RF waves. Modified version of picture from [26].

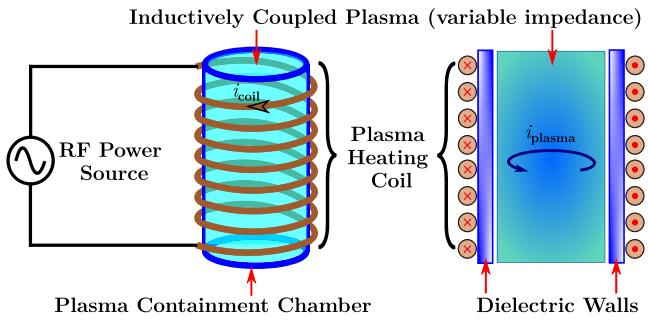

Fig. 6. Solenoidal inductively coupled plasma (ICP) coil, surrounding a plasma chamber. The RF power source drives RF currents in the plasma.

plasma chamber, or as a solenoidal coil wound around the chamber. The plasma inside the chamber couples inductively with the adjacent coil when an RF current is driven in the coil, leading to an RF current being induced inside the plasma and, in turn, an inductive transfer of power from the coil to the plasma, similar to the operation of a transformer. These are referred to as ICP sources and have been used extensively in the semiconductor industry, as well as in ion accelerators (CERN LINAC4), as they provide advantages such as high plasma density and ease of scalability [29]. In Fig. 6, a solenoidal coil ICP is shown. ICPs require HF to VHF currents to be driven through the antenna to inductively transfer heat to the coupled plasma. These currents must be very large to inductively transfer a substantial amount of power into the plasma.

Traditional microwave plasma heating systems are usually implemented with highly specialized high-power linear-beam

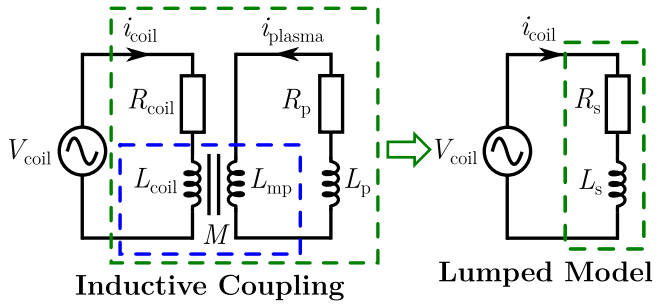

Fig. 7. Transformer model of the inductively coupled plasma (ICP) system. This model can be simplified into a lumped model with a total resistance R_s and total inductance L_s.

vacuum tubes, such as gyrotrons, in combination with high voltage high power semiconductor devices such as IGBTs. The system is highly customized, expensive, not scalable, and difficult to maintain. ICPs, on the other hand, can be operated using multiple power electronic amplifiers connected together in a tree structure using power combiners, as shown in Fig. 3. By aggregating multiple small-power power electronic amplifiers as a modular, scalable, high-voltage and high-power unit, the modularity and scalability of the plasma heating systems can be greatly improved. This approach also allows emerging low-voltage, low-power rating wide-band-gap (WBG) power semiconductor devices (e.g., SiC and GaN), originally designed for high-volume, cost sensitive commodity applications such as electric vehicles and grid-interface inverters, being used for specialized high-voltage, high-power applications such as fusion plasma heating, which has the potential to significantly reduce the overall cost of the system.

III. Impedance of Inductively Coupled Plasma

The solenoidal ICP, introduced in Fig. 6, is used as the example load for this article. The equivalent electric circuit model of the ICP can be visualized as a transformer, as shown in Fig. 7. This transformer model has been previously introduced and defined extensively in [30], [31], [32], [33], [34]. R_{coil} and L_{coil} represent the self-resistance and inductance of the RF coil, without considering the plasma chamber. The plasma can be considered to have its own resistance R_p and inductance L_p, which are variable, and the plasma is inductively coupled to the antenna (coil). The current flowing in the coil induces a current in the plasma through an additional coupling inductance L_{mp}. This transformer model can be converted into a lumped model, with an equivalent total resistance R_s and total inductance L_s of the ICP. The equations detailing the transformer model of the ICP have been provided in the Appendix (A.1)–(A.6). More details for the rationale behind the equivalent transformer model of Fig. 7 and the related equations can be found in [30], [31], [32], [33], and [34].

The impedance variation of an ICP reactor can be estimated fairly accurately using these equations, for particular values of the ICP dimensions and plasma characteristics, namely the plasma electron density and the electron collision frequency,

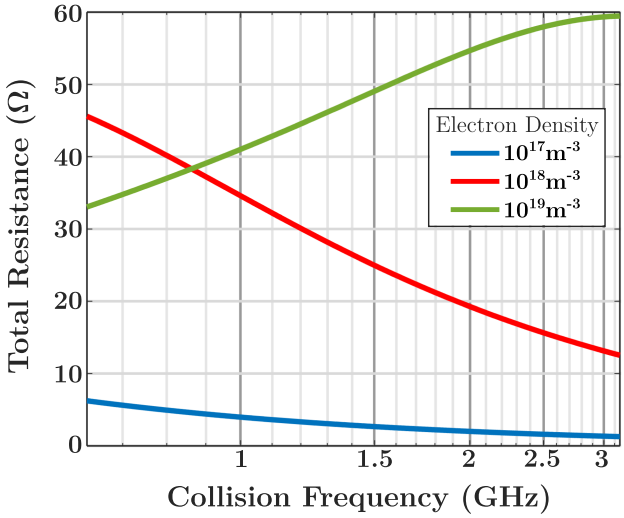

Fig. 8. Resistance variation of an ICP with respect to electron collision frequencies in the high pressure regime, for different plasma electron densities when driven by a 10 MHz RF current.

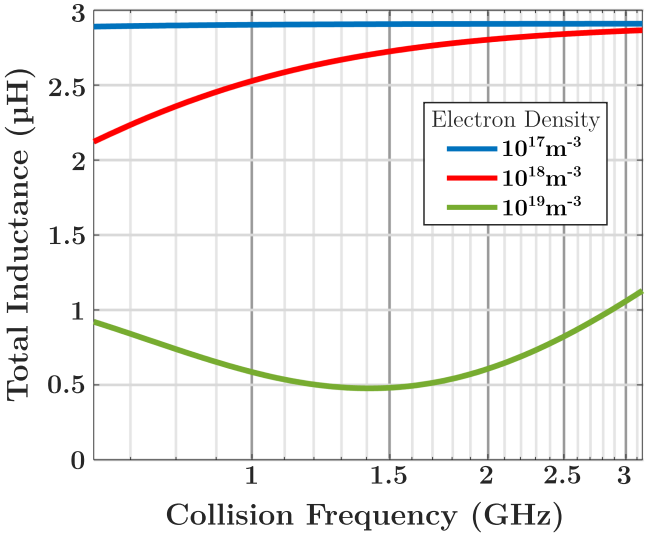

Fig. 9. Inductance variation of an ICP with respect to electron collision frequencies in the high pressure regime, for different plasma electron densities when driven by a 10 MHz RF current.

which strongly influence the operation of the ICP. The example ICP reactor considered in this article has chamber dimensions as 30 cm, 32 cm, and 50 cm for r_0, r_c and l, respectively. The external solenoidal coil wound around the plasma chamber has $N = 6$ turns. The variation of this ICP reactor's resistance and inductance, for different values of the plasma electron density and electron collision frequency are presented in Figs. 8 and 9, respectively. The total resistance and total inductance values shown in these figures indicate the analytically calculated values of R_s and L_s for the lumped model of the ICP shown in Fig. 7. It can be seen that for different electron densities, both the resistance and the inductance of the ICP reactor show marked variation and trend of change. For example, the resistance of the ICP shows a decreasing trend with increasing collision

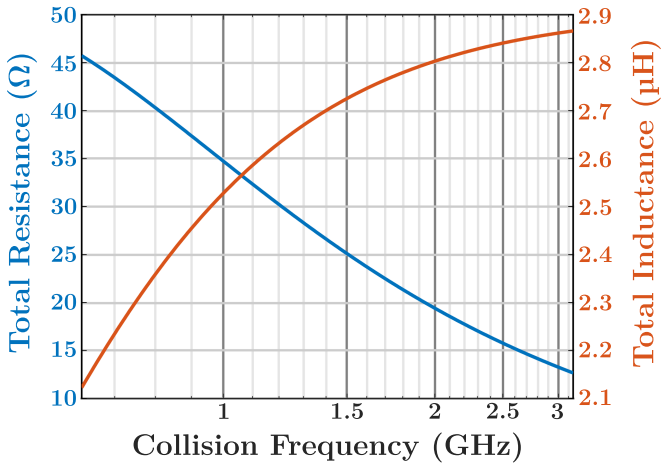

Fig. 10. Resistance and inductance variation of an ICP over the considered electron collision frequency range at a plasma electron density of 10^{18} m^{-3} when driven by a 10 MHz RF current.

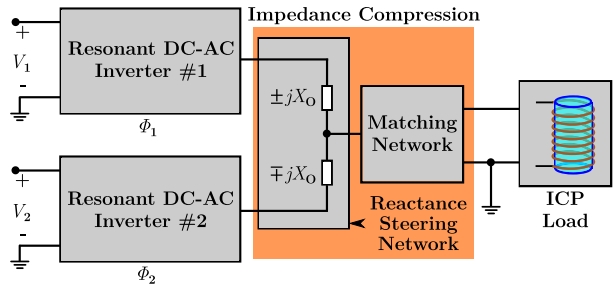

Fig. 11. ICP load driven by two Class-E inverters connected in parallel via a Reactance Steering Network (RSN) and an impedance matching network.

frequency, for the plasma electron densities of 10^{17} m^{-3} and 10^{18} m^{-3}, while it shows the opposite trend for an electron density of 10^{19} m^{-3}.

Thus, it can be inferred from Figs. 8 and 9 that the impedance of the ICP reactor is greatly affected by both the electron density and collision frequency of the plasma. Usually, the electron density of the plasma stays constant during the operation of the ICP. Therefore, for this article, the electron density of the plasma contained inside the chamber was assumed to be relatively constant at around 10^{18} m^{-3}, as this is a standard value of electron density for most conventional ICP reactors [35], [36]. On the other hand, the electron collision frequency of the plasma inside the reactor changes with the plasma temperature and pressure. As more energy is transferred inductively to the plasma inside an ICP during operation, its temperature and pressure increases, which in turn increases the collision frequency of the electrons inside the plasma. Hence, during conventional operation, the variable impedance invariably results due to the changing plasma electron collision frequency. The variation of the resistance and reactance of the ICP load has been presented with respect to a range of electron collision frequencies, since that is the expected trend of variation of the plasma impedance with operation over time and the same convention has been followed in the rest of the article.

A 10 MHz sinusoidal current is taken as the driving current for the ICP coil. 10 MHz was selected as a representative frequency for studying RF heating of ICP plasmas when operating in the high plasma pressure regime. The variation in the resistance and inductance of this particular ICP reactor with respect to the electron collision frequency is presented in Fig. 10. Both resistance and inductance show considerable variation with the collision frequency in the high plasma pressure regime ($\nu_m \gg \omega$), given that a 10 MHz simusoidal curent is driving the ICP coil. As the collision frequency changes from 0.5 to 3 GHz, the effective resistance of the plasma shows a monotonical decrease from 46 Ω to 13 Ω, while the effective inductance increases from around 2.15 μH to 2.85 μH. This highlights the large variation in the impedance of the ICP during operation, which is detrimental to high-frequency resonant power amplifiers such as Class E, as such power amplifiers require small output impedance variation. Therefore, the use of a matching network and a reactance steering network along with dynamic phase shift and input voltage variations according to operational load variation becomes warranted, so that this large variation in the load impedance can be minimized, thus increasing the desirable range of operation for high-frequency resonant power amplifiers.

IV. Power Combining Network Design

As presented in the previous section, due to the large range of variance of the impedance of an ICP reactor, the need arises to compress this impedance variation to a smaller range, such that the ZVS operation of high-frequency resonant inverters can be ensured for almost the entire range when driving such loads. In this approach, the RSN is used together with a dedicated single-stage L-shaped matching network, to connect two Class E inverters in parallel to the ICP load. The advantage of this approach is that: 1) more power can be delivered to the load since two inverters are connected in parallel; and 2) through compensatory action between the two inverters, any variation in the effective output load impedance can be accounted for. A block diagram of the conceptual circuit architecture is shown in Fig. 11. The following two subsections describe the design procedure for the RSN and the matching network.

A. Matching Network Design

To compress the impedance variation seen at the output terminal of the RSN, a matching network is added in between the RSN and the ICP load in the proposed power amplifier architecture. Note that the RSN is capable of handling variable loads. However, the addition of the matching network allows for further compression of the output impedance which makes it possible to realize the RSN with smaller values of the reactive components. The matching network also helps to reduce the incidence of ac power reflection, by matching the input impedance of the matching network to be equal to a desired source impedance [24], [31].

To keep the number of passive components used in the design of the circuit low, a single stage *LC*-matching network is used. This includes a series capacitor followed by an inductor in

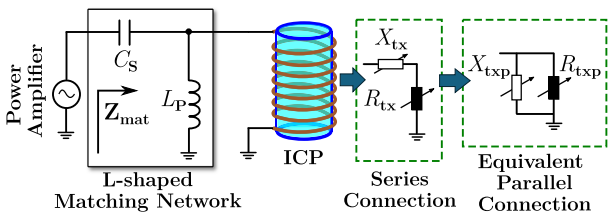

Fig. 12. Circuit diagram depicting the ICP load connected to the power amplifier circuit via a matching network.

parallel with the load as shown in Fig. 12, which acts as a high-pass filter. As shown previously, the ICP reactor can be modeled as a variable series inductive load. The single-stage matching network is designed according to a selected reference impedance point among the range of impedances of the ICP load, which is matched to a desired source impedance. A prudent choice for this reference point Z_{ref}, is a point on the impedance curve of the ICP, where the impedance is close to or equal to the geometric mean of the maximum and minimum values of the impedance range (Z_{max}, Z_{min}), i.e.,

$$Z_{\text{ref}} = \sqrt{Z_{\text{max}} Z_{\text{min}}}. \tag{1}$$

The *vvvvvv*-matching network used for this system is designed based on this reference output impedance of Z_{ref}. The design equations for the matching network are provided in Appendix A2. For the example ICP reactor considered in this article, the values of Z_{max} and Z_{min} are 180.5 Ω and 141 Ω. Using (1), the value of Z_{ref} for this case is 159.5 Ω. Hence, the load point (38.4 Ω, 2.42 μH) on the ICP's impedance curve, shown in Fig. 10, with an impedance of 157 Ω, which is in the vicinity of the calculated value of Z_{ref}. The single-stage high-pass matching network is then designed for a range of source impedance values from 5 Ω to 20 Ω. These values allow for a realizable matching network design with good Q-factors for the passive components. Such a range also ensures that Q_{P} is greater than Q_{PL} at Z_{ref}, allowing for realizable values of L_{P} according to (A.12). In the end, the matching network design with component values $L_{\text{P}} = 3.74$ μH and $C_{\text{S}} = 170$ pF for an R_{S} of 14 Ω is chosen. This design provides good impedance compression, as well as having an acceptable 3 dB frequency for the desired 10 MHz operation of the system. More importantly, for this matching network, the design constraints on the RSN are satisfied. $|X_{\text{txm}}|_{\text{max}} < \sqrt{(X_{\text{txm}}^2 + R_{\text{txm}}^2)_{\text{min}}}$ over the entire range of the matched load (considering R_{txm} and X_{txm} refer to the resistance and reactance value of the matched load, respectively). This allows for a realizable RSN design, as will be shown in the next subsection.

Fig. 13 shows the effect of the designed matching network on the impedance variation of the ICP load. The dashed lines represent the ICP's original total resistance (R_{s}) and reactance values (ωL_{s}) for the entire range of electron collision frequencies considered. Simultaneously, the solid lines depict the variation of the resistance and reactance values of the ICP together with the designed matching network, which is the effective impedance Z_{mat} seen at the input of the matching network, as shown in

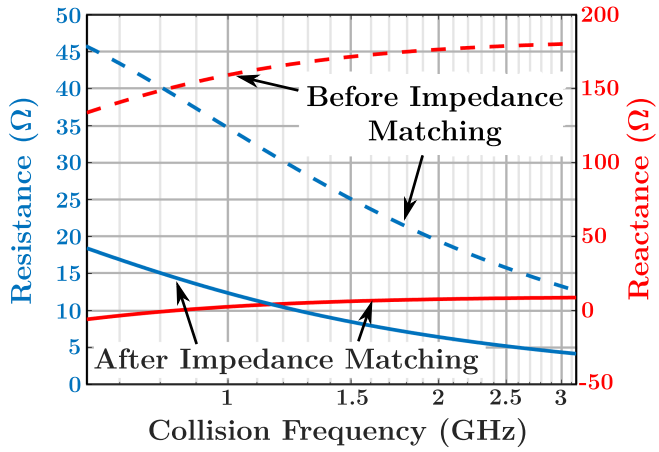

Fig. 13. Achieved impedance compression after the addition of a high-pass L-shape matching network. The resistance and reactance ranges of the matched load Z_{mat} are compressed considerably.

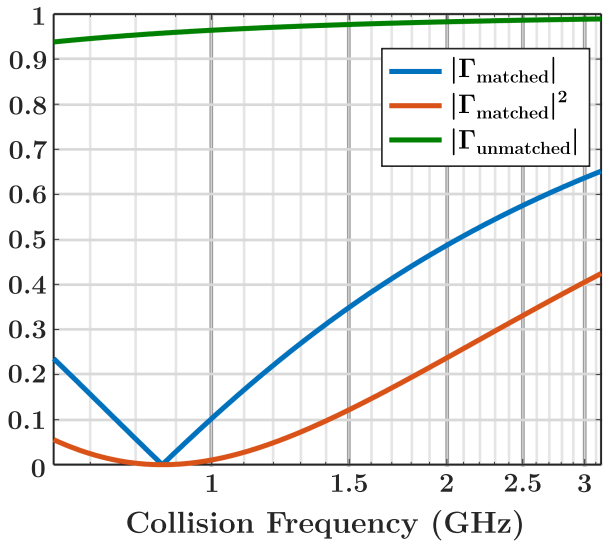

Fig. 14. Effect of the addition of the matching network on the power reflection co-efficient $|\Gamma|$ and the power reflection ratio $|\Gamma_{matched}|^2$, with respect to a 14 Ω source impedance.

Fig. 12. The matching network compresses the range of variation of the output resistance and reactance. The output resistance of the ICP reactor initially varies from 45.7 Ω to 18.3 Ω, which is compressed by the matching network to lie between 12.7 Ω and 4.1 Ω. At the same time, the load reactance values are greatly compressed. The range of the reactance change from 134.5 Ω and 180.1 Ω before matching to –6.4 Ω and 8.3 Ω after the matching network. In addition, the ICP reactor is always inductive in nature over the entire range of collision frequencies, however, after adding the matching network, the effective impedance is capacitive for some part of the considered range and inductive for the other part. This small range of variation of the effective load reactance Z_{mat} makes the design of the RSN more feasible.

Fig. 14 highlights the impact of the matching network in reducing the power reflection co-efficient for all load points of the ICP reactor load. The power reflection coefficient Γ is

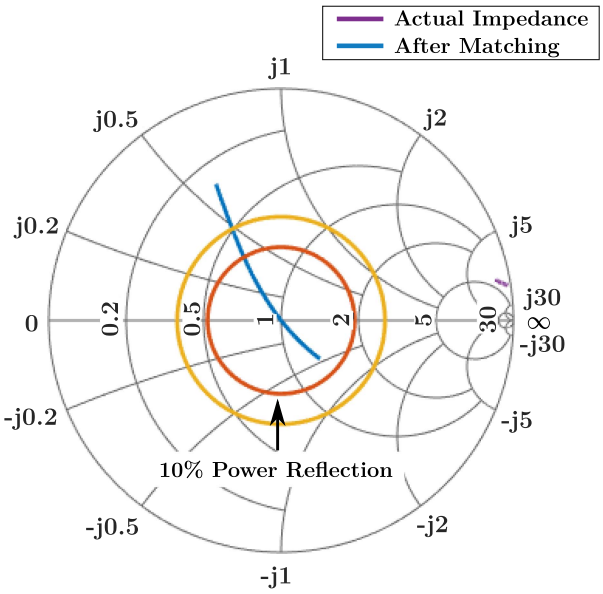

Fig. 15. Smith chart showing the effect of the addition of the matching network on the power absorption ratio, with respect to a 14 Ω source impedance.

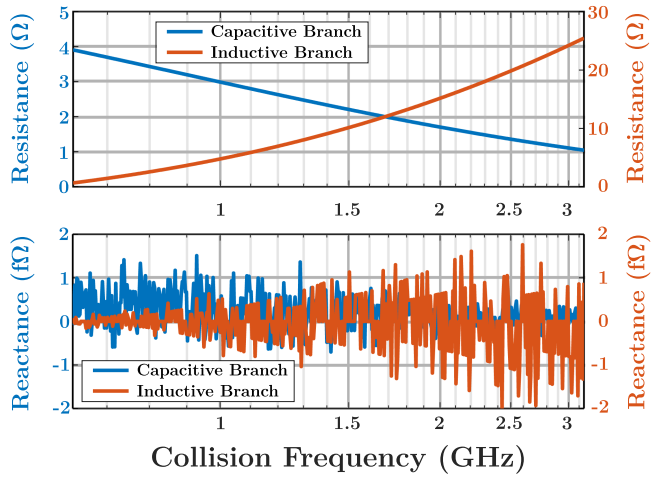

Fig. 16. Variation in the resistive and reactive components of the output impedances seen by the Class E inverters due to the effect of the RSN (both K_{LC} and ϕ_{LC} and varied). The reactance is negligible, while the variation in the resistive part is also small.

calculated according to the following equation:

$$\Gamma = \frac{Z_{\mathrm{L}} - Z_{\mathrm{O}}}{Z_{\mathrm{L}} + Z_{\mathrm{O}}} \tag{2}$$

where Z_{L} and Z_{O} signify the load impedance and the source impedance or the transmission line impedance. Prior to the matching network, the ICP reactor impedance has a value of $|\Gamma|$ larger than 0.9 for all points, when connected to a source impedance of 14 Ω. This implies that if the circuit is directly connected to the ICP reactor without any matching network, most of the power is going to get reflected back to the source. After the addition of the matching network, the power reflection coefficient of the effective load reduces, corresponding to the same source impedance. The parameter $|\Gamma_{matched}|^2$ defines the ratio of the input power reflected back to the source, after the addition of the matching network. It can be seen that for most load points, less than 20% of the power is reflected back, with the worst case value being close to 40%. On the other hand, the smith chart presented in Fig. 15 shows the power absorption ratio $(1 - |\Gamma_{matched}|^2)$ of the matched ICP reactor for all load points. After adding the matching network, the load point that is matched to the source impedance value has an absorption ratio of 1, which implies that all power is transferred from the source to the load without reflection. Moreover, the power reflection at all load points is less than 10% for most load points for the matched load, whereas the original load curve, denoted in purple, has greater than 90% power reflection at all points.

B. Reactance Steering Network Design

The RSN consists of two parallel branches and aims to minimize the variation in the reactance seen at the output terminals of the inverters connected to the RSN by managing the power driven through the two branches of the RSN by the inverters. These two branches are called the capacitive branch and the inductive branch. The capacitive branch consists of a capacitor with reactance $-jX_{\mathrm{C}}$, while the inductive branch has an inductor with reactance jX_{L}. For an inductive load, more power is driven through the inverter connected to the capacitive branch to compensate for the inductive part of the load, and vice versa. Thus, the power flow through both branches can be controlled such that the output impedances Z_{C} and Z_{L} seen by the inverters connected to the two RSN branches are almost purely resistive, which is important for ensuring Zero Voltage Switching (ZVS) operation for the connected resonant Class-E inverters, especially in the MHz range [37]. The reactances of the two branches can be selected to be equal to simplify the mathematical analysis of the RSN network ($X_{\mathrm{C}} = X_{\mathrm{L}} = X_{\mathrm{O}}$). The branch output impedances Z_{C} and Z_{L} are given as

$$Z_{\mathrm{C}} = \frac{X_{\mathrm{O}}^2}{R_{\mathrm{txm}} - K_{\mathrm{LC}}^* R_{\mathrm{txm}} + j(X_{\mathrm{txm}} + X_{\mathrm{O}} - K_{\mathrm{LC}}^* X_{\mathrm{txm}})}. \tag{3}$$

$$Z_{\mathrm{L}} = \frac{X_{\mathrm{O}}^2}{R_{\mathrm{txm}} - \frac{1}{K_{\mathrm{LC}}^*} R_{\mathrm{txm}} + j(X_{\mathrm{txm}} - X_{\mathrm{O}} - \frac{1}{K_{\mathrm{LC}}^*} X_{\mathrm{txm}})}. \tag{4}$$

Here, K_{LC}^* is the complex voltage ratio between the inductive and capacitive branch input voltages ($K_{\mathrm{LC}}^* = \frac{V_{\mathrm{L}}}{V_{\mathrm{C}}} e^{j(\phi_{\mathrm{L}} - \phi_{\mathrm{C}})}$). Moreover, R_{txm} and X_{txm} refer to the resistive and reactive component of the matched load, shown in Fig. 13. Z_{C} and Z_{L} can be made to appear resistive by modulating the ratio of the input dc voltages ($V_L/V_C = K_{\mathrm{LC}}$), as well as the phase shift between the two inverters ($\phi_{\mathrm{LC}} = \phi_{\mathrm{L}} - \phi_{\mathrm{C}}$). This is a feature of the RSN, in comparison to Chireix outphasing power combiners [38], [39], where only the phase-shift between inverters is varied. Since Z_{C} and Z_{L} are functions of K_{LC}, as shown in (3) and (4), and since K_{LC} itself is a function of ϕ_{LC}, the operation of the RSN is intertwined with both K_{LC} and ϕ_{LC}. The governing equations

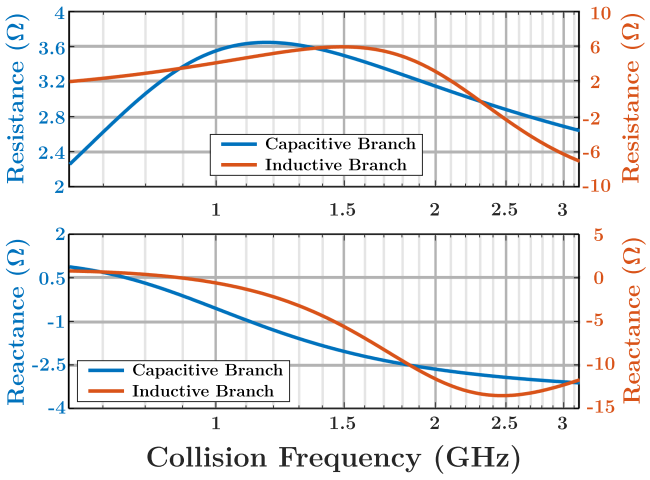

Fig. 17. Variation in the resistive and reactive components of the output impedances seen by the Class E inverters due to the effect of the RSN (both $K_{\mathrm{LC}} = 1$, only ϕ_{LC} is varied). When only employing phase shift control, the reactance is no longer compressed to zero.

for K_{LC} and ϕ_{LC} for resistive Z_{C} and Z_{L} are

$$K_{\mathrm{LC}} = \frac{X_{\mathrm{txm}}\cos(\phi_{\mathrm{LC}}) - R_{\mathrm{txm}}\sin(\phi_{\mathrm{LC}})}{X_{\mathrm{txm}} - X_{\mathrm{O}}}. \tag{5}$$

$$\sin^2\phi_{\mathrm{LC}} = \frac{X_{\mathrm{O}}^2}{X_{\mathrm{txm}}^2 + R_{\mathrm{txm}}^2}. \tag{6}$$

The denominator of (5) suggests that the value of X_{O} should not be equal to the effective load reactance X_{txm}, otherwise the value of K_{LC} would be undefined. (6) indicates that ϕ_{LC} can have a value in all four quadrants, which can lead to different values of K_{LC} and hence create different usable combinations of ϕ_{LC} and K_{LC} for any given load. However, to avoid multiple solutions and to have a one-to-one relation, we use values of ϕ_{LC} in the second quadrant only, as these values of ϕ_{LC}, together with the corresponding values of K_{LC}, help to significantly compress the effective impedance seen at the output terminals of the two resonant inverters. Moreover, from (6), a real value for ϕ_{LC} will result if and only if X_{O}^2 is less than or equal $X_{\mathrm{txm}}^2 + R_{\mathrm{txm}}^2$, which is the square of the impedance of the matched output load. Thus, for a variable output impedance, the following two constraints are applied to the value of X_{O}:

$$|X_{\mathrm{O}}| > |X_{\mathrm{txm}}|_{\max}. \tag{7}$$

$$|X_{\mathrm{O}}| \leq \sqrt{(X_{\mathrm{txm}}^2 + R_{\mathrm{txm}}^2)_{\min}}. \tag{8}$$

The aforementioned constraints place upper and lower bounds for the value of X_{O}. Selecting a value for $|X_{\mathrm{O}}|$ greater than $|X_{\mathrm{txm}}|_{\max}$ results in a well-defined value for K_{LC}, while satisfying constraint (8) ensures that values of ϕ_{LC} obtained over the entire range of impedances considered are all real. However, $|X_{\mathrm{txm}}|_{\max}$ must be less than $\sqrt{(X_{\mathrm{txm}}^2 + R_{\mathrm{txm}}^2)_{\min}}$, otherwise no realizable RSN design exists, and the matching network would need to be redesigned again. The maximum value of $|X_{\mathrm{txm}}|$ for the matched ICP reactor load is 8.291 Ω, while the minimum

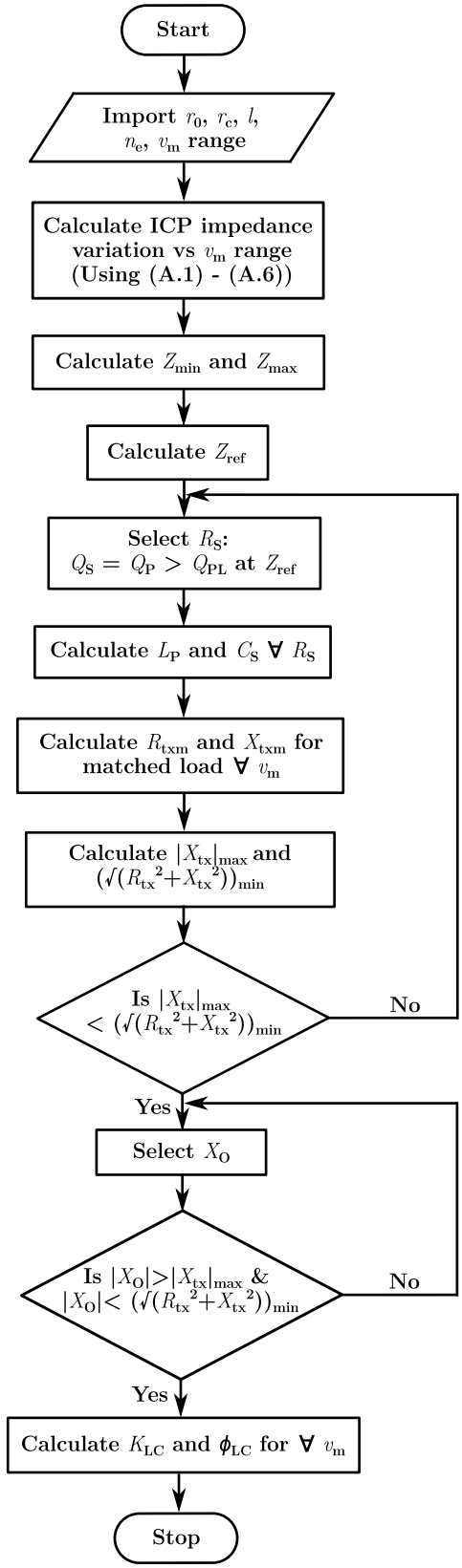

Fig. 18. Flowchart showing the design process of the RSN and the matching network for the variable impedance ICP load.

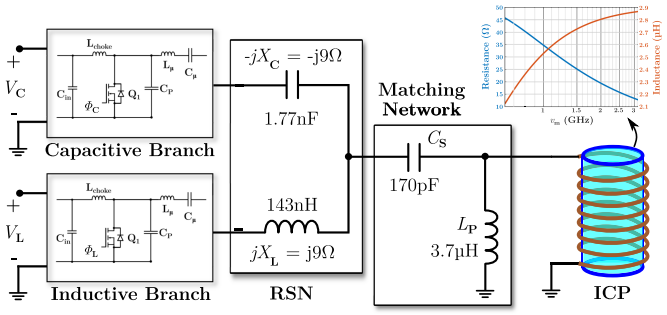

Fig. 19. Circuit diagram depicting the impedance matched ICP load driven by two equivalent resonant Class-E inverters connected in parallel via the designed Reactance Steering Network (RSN).

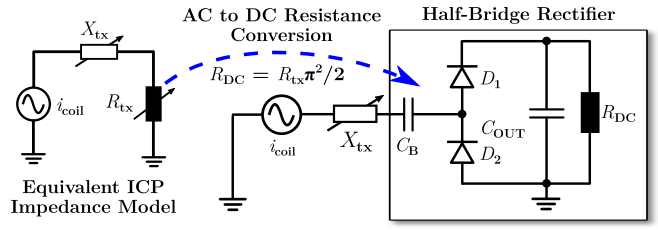

Fig. 20. Inductive ICP load is modeled as a DC resistance connected to an AC source by means of a half-bridge rectifier and a series inductance.

value of $\sqrt{X_{\text{txm}}^2 + R_{\text{txm}}^2}$ is 9.231 Ω. Therefore, for this case, $|X_{\text{O}}|$ is selected as 9 Ω. Fig. 16 shows the effect of the RSN with a value of $X_{\text{O}} = X_{\text{C}} = X_{\text{L}} = 9\,\Omega$ on the effective load impedance shown in Fig. 13, with appropriate values of K_{LC} and ϕ_{LC}. The impedances seen by the Class E inverters are almost completely resistive with the reactive parts having magnitudes in the range of $10^{-15}\,\Omega$ (fΩ). This is crucial for high-frequency operation as switching losses, which increase with switching frequency, are almost completely eliminated by ZVS operation. This is in stark contrast to the case if only phase shift ϕ_{LC} variation is employed. As can be seen from Fig. 17, the reactance seen at the output terminals of the two Class E inverters is no longer compressed to zero, which negatively impacts ZVS operation and hence reduces overall system efficiency. This highlights the advantage of employing the RSN for reactance cancellation with both phase-shift and input voltage ratio modulation over the conventionally used phase outphasing techniques.

In addition, the resistance of the inductive branch is smaller in magnitude than the capacitive branch when the effective load impedance is capacitive in nature, which implies that more power is drawn from the inductive branch to compensate for the capacitive behavior of the load. Similarly, for the region where the load is inductive, the resistance of the capacitive branch is larger. This shows that the RSN works to drive more power through the branch which compensates for the reactive nature of the effective load impedance seen at the output of the RSN in this case.

Using the matching network and the RSN designs presented in the previous subsections, the entire topology of the high-frequency resonant converter circuit for driving ICP reactor loads is realized. A flowchart has been provided in Fig. 18 to showcase the sequence of design steps followed for deciding on the component values of the matching network and RSN for a particular ICP load.

V. Simulations and Experimental Verification

The high-frequency resonant power amplifier circuit, intended for driving the ICP reactor load, is framed with the component values of the matching network and the RSN as given in the previous section. The circuit diagram of this proposed ICP driver circuit is presented in Fig. 19. Since the ICP reactor load can in effect be considered as a variable series inductive load driven by RF currents, as previously shown in the lumped model of Fig. 7, it can therefore be modeled as a separate variable inductance connected in series to a variable dc resistance, by means of half-bridge rectifier. A representation of the load circuit conversion from an ac load to a dc load is shown in Fig. 20. The series reactance X_{tx} models the inductive part of the ICP load, while the dc load R_{DC} is selected such that it equals the resistive part of the ICP load, after the resistance conversion ratio of the half-bridge rectifier is applied. The inductance and dc resistance values are selected such that the impedance of the equivalent load circuit shows a pattern of variation similar to that of the analytically calculated impedance of the ICP reactor, shown in Fig. 9. Moreover, the ac load is converted to a dc load to accurately record the efficiency of the designed ICP driver circuit. The addition of the rectifier circuit adds additional device losses, which can be removed from the loss calculations to gauge the overall dc-ac power conversion of the designed circuit.

TABLE I
Component Values of the Class E Inverters in the Capacitive and Inductive Branches

Branch	C_{in}	L_{choke}	C_{P}	L_{μ}	C_{μ}
Capacitive	18.8 μF	6.5 μH	400 pF	1.01 μH	214 pF
Inductive	18.8 μF	6.5 μH	400 pF	1.15 μH	307 pF

The Class E inverters connected to the capacitive branch and inductive branch of the RSN are equivalent to each other and are designed with similar components to ensure that both inverters operate at the same switching frequency of 10 MHz, with ZVS. Thus, the outputs of both these inverters are 10 MHz RF currents. The circuit parameters for the Class E inverters are provided in Table I. C_{in}, L_{choke} and C_{P} specify the values of the input capacitance, choke inductance and the external capacitance placed parallel to the switch, and both inverters have the same values for these parameters. The series resonant tank of the inverters are formed by L_{μ} and C_{μ} and they are tuned to be resonant at 10 MHz. Since the passive components making up the RSN are merged together with the respective series resonant tanks, the values of L_{μ} and C_{μ} are different for the two inverters.

The designed driver circuit was first simulated in PLECS, using the parameter values specified previously, to verify its effectiveness in driving variable impedance ICP reactor loads. The ICP is modeled as a series inductive load, with an ideal inductor in series with a dc resistance via a half-bridge rectifier,

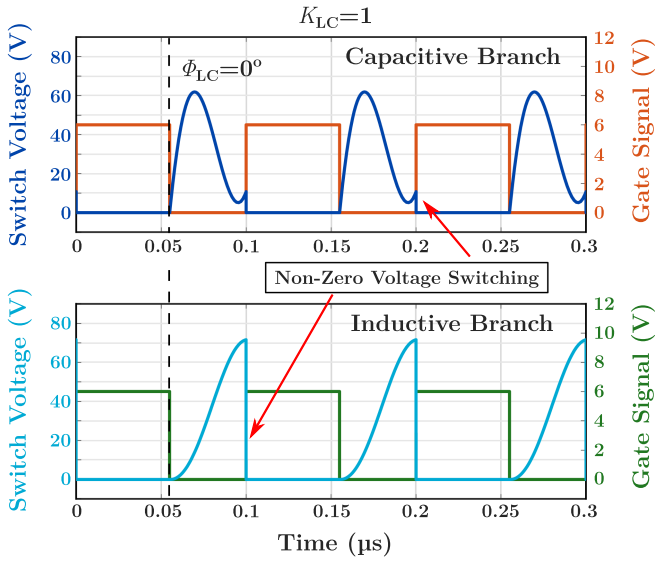

Fig. 21. Simulation results showing non-ZVS operation for the ICP driver circuit when supplying a load with $R_{DC} = 190\,\Omega$ and $L_{tx} = 2.42\,\mu$H at 10 MHz. $K_{LC} = 1$ and $\phi_{LC} = 0°$.

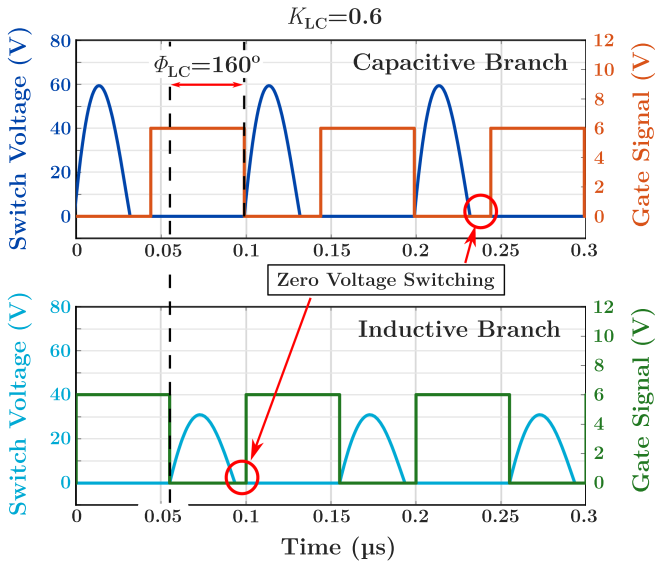

Fig. 22. Simulation results showing ZVS operation for the ICP driver circuit when supplying a load with $R_{DC} = 190\,\Omega$ and $L_{tx} = 2.42\,\mu$H at 10 MHz. $K_{LC} = 0.6$ and $\phi_{LC} = 160°$ ensure ZVS operation.

as shown in Fig. 20. The semiconductor devices are assumed to be ideal devices in these simulations. A number of load points were selected from the impedance curve for the ICP for simulations. The circuit behavior was tested for each of these load points. It was found that by properly selecting the values of K_{LC} and ϕ_{LC} according to the RSN equations (5) and (6), ZVS operation can be ensured for both Class E inverters. The results for one particular simulation case are shown in Figs. 21 and 22. The dc resistance value and the series inductance values were $R_{DC} = 190\,\Omega$ and $L_{tx} = 2.42\,\mu$H, respectively. This corresponds to a load point on the ICP impedance curve of R_{ICP} $= 38.5\,\Omega$ and $L_{ICP} = 2.42\,\mu$H. The switch duty ratio for both inverters was selected as $D = 0.55$ at a switching frequency of 10 MHz. Fig. 21 shows the system operation results with $K_{LC} = 1$ and $\phi_{LC} = 0°$, that is, when the RSN equations are not used. As a result, both Class E inverters exhibit non-ZVS switching. However, when the system is operated with proper values of $K_{LC} = 0.6$ and $\phi_{LC} = 160°$, both Class E inverters show ZVS. The results for this desired mode of operation are shown in Fig. 22. Similar results were observed for the simulations performed for different values of the emulated ICP reactor load, when the circuit was driven with proper values of K_{LC} and ϕ_{LC}.

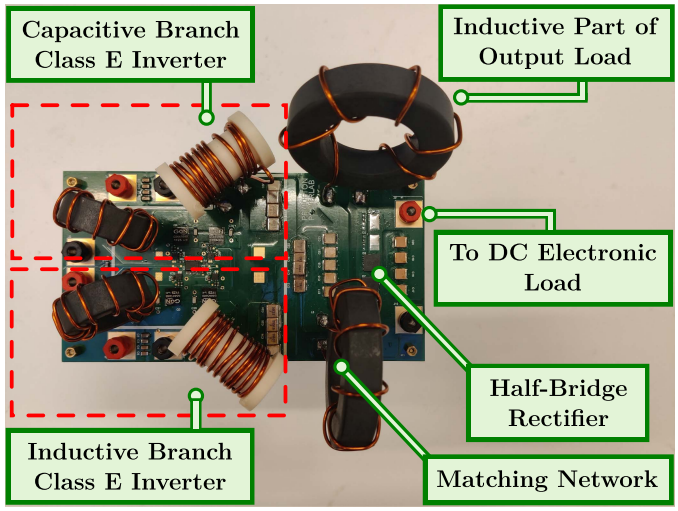

Fig. 23. Image of the hardware prototype of the proposed ICP driver circuit.

The same circuit was also implemented on hardware for experimental verification, and this experimental prototype shown in Fig. 23. The series resonant tank inductances of the Class E inverters, L_μ, were chosen to be wire-wound air-core inductances. The small values of these inductances allows for an air-core design. Moreover, these inductances see a large voltage drop across themselves, usually at larger powers. Using air-core inductors completely eliminates the problem of core saturation for these inductors. The input choke inductances L_{choke}, the matching network inductance L_P as well as the load inductance L_{tx}, were implemented in hardware as cored inductances. The large values of these inductances as well as a comparatively lower voltage drop allows for a cored inductor implementation without the risk of core saturation. The core material for these inductances was chosen as the Fair-rite 67 material, which has good permeability in the HF regime. An HP 6063B dc electronic load was used as the dc output resistance R_{DC} of the system. The switch used for the two Class E inverters was the GS66508B 650 V/30 A GaN MOSFET provided by GaN Systems. These switches were bottom cooled through thermal vias and heat sinks. 650 V rated devices are used since the peak drain to source voltage across the switches may go beyond 200 V at full load operation, with higher peak voltages during transients. Moreover, using these devices allows for testing the system for a variety of operating conditions at the cost of a slightly reduced efficiency.

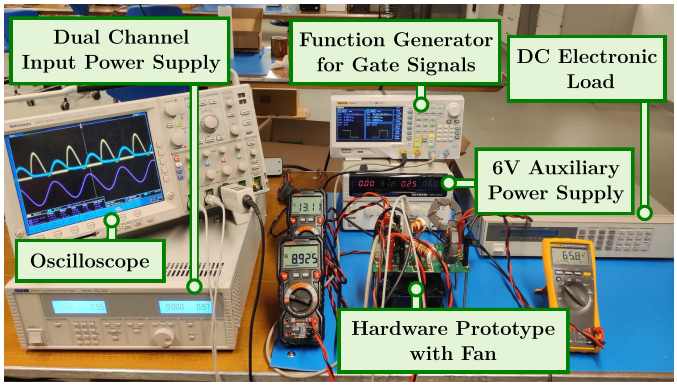

Fig. 24. Complete hardware setup for the proposed ICP driver circuit.

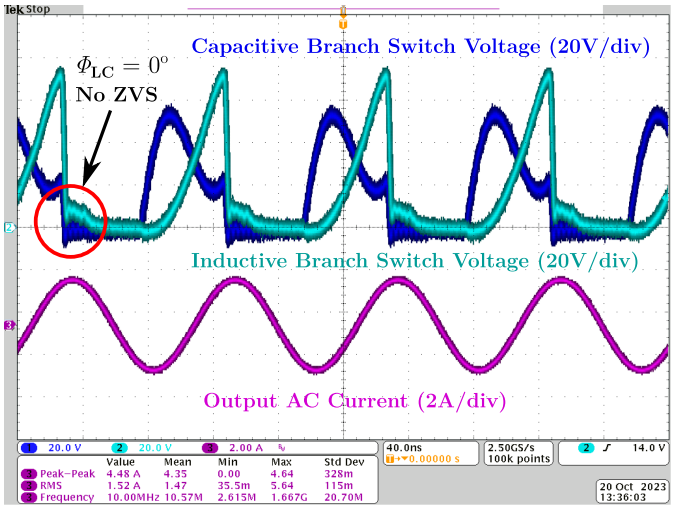

Fig. 25. Experimental results showing the hard-switched switch voltages of the Class E inverters and the output inductor current, with $K_{LC} = 0.91$ and $\phi_{LC} = 0°$, when driving a load $R_{DC} = 150\,\Omega$ and $L_{tx} = 2.33\,\mu$H at 10 MHz, for an output power of 20.5 W.

The 10 MHz square wave gate signals for these switches were provided through a RIGOL DG4102 function generator. The half-bridge rectifier diodes on the load side were 650V/20A SiC Schottky diodes (FFSM2065B) provided by Onsemi. C0G capacitances were used for the series resonant tank capacitors of the Class E inverters as well as for the matching network capacitor, due to their small temperature variation coefficient. The entire hardware test setup is shown in Fig. 24. This setup was used to carry out a number of experiments for validating the operation of the designed ICP driver circuit.

A. Operation With and Without Zero Voltage Switching (ZVS)

Similar to one of the simulations, the designed resonant power amplifier circuit was set up to drive a dc load of $R_{DC} = 150\,\Omega$ with and inductance of $L_{tx} = 2.33\,\mu$H in series, without any phase shift between the two branches ($\phi_{LC} = 0°$). The experimental results for this case are shown in Fig. 25. The switch voltage waveforms for the capacitive and inductive branch Class E inverters show hard-switching or non ZVS operation. The

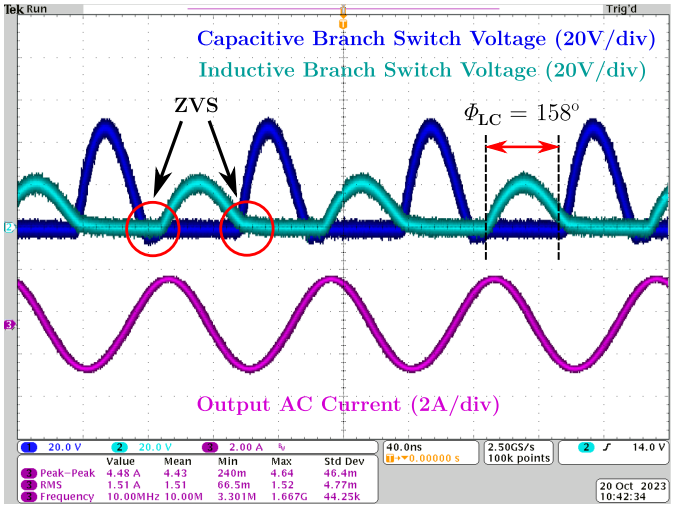

Fig. 26. Experimental results showing the ZVS switch voltages of the Class E inverters the output inductor current, with $K_{LC} = 0.61$ and $\phi_{LC} = 158°$, when driving a load $R_{DC} = 150\,\Omega$ and $L_{tx} = 2.33\,\mu$H at 10 MHz, for an output power of 20.5 W.

voltages provided at the inputs of the capacitive branch and inductive branch Class E inverters, V_C and V_L, are 16.5 V and 15 V, respectively, with $K_{LC} = V_L/V_C = 0.91$. A sinusoidal RF current at 10 MHz with an rms value of 1.52 A flows through the output inductance L_{tx}. The circuit provides an active power of 20.5 W to R_{DC} at an output voltage of 55.6 V, at an efficiency of 37.25%. In addition, almost all of the power is supplied by the capacitive branch Class E inverter, with the inductive branch voltage source being in an idle state, which shows a very imbalanced mode of operation.

On the other hand, the experimental results for the case when the circuit drives the same load with proper values of K_{LC} and ϕ_{LC} are presented in Fig. 26. For $\phi_{LC} = 158°$, and $K_{LC} = 0.61$, the switches of the Class E inverters in both branches operate in ZVS. A similar sinusoidal RF current with an rms value of 1.51 A flows through the output inductance L_{tx}. As a result, the circuit again provides 20.5 W of power to R_{DC} at an output voltage of 55.6 V, but at an efficiency of 66%, due to ZVS. The input voltages, V_C and V_L, are 11.4 V and 6.9 V, respectively, and both branches provide power to the output load. Thus, these simulation and experimental results highlight the importance of selecting the proper values of ϕ_{LC}, and K_{LC}, for the designed ICP driver circuit to operate more efficiently. For both these cases, the switches were driven with gate signals at a frequency of 10 MHz with $D = 0.5$.

B. Full Load Operation

In the next experiment, the designed circuit was driven at full power for the same equivalent dc load of $R_{DC} = 150\,\Omega$ and a series inductance of $L_{tx} = 2.33\,\mu$H. The value of K_{LC} for this case was 0.78, with the capacitive branch and inductive branch input voltages V_C and V_L being 35.5 V and 27.8 V, respectively. This indicates that the inductive branch provided more power than the capacitive branch, which is aligned with the expected behavior.

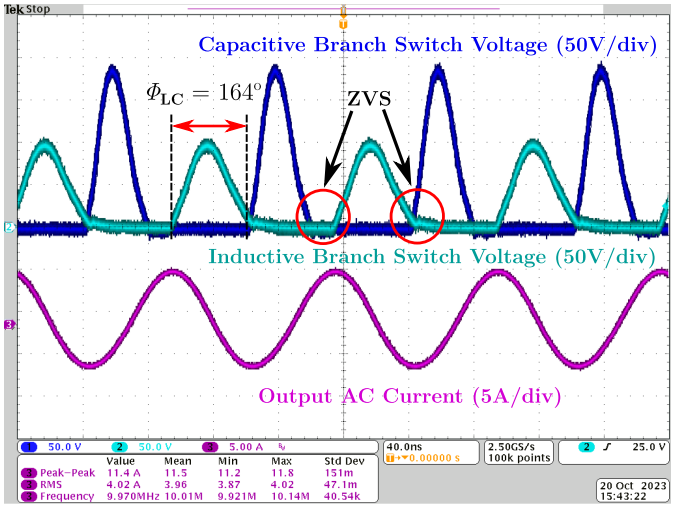

Fig. 27. Experimental results with $K_{LC} = 0.8$ and $\phi_{LC} = 164°$, when driving a load $R_{DC} = 150\,\Omega$ and $L_{tx} = 2.33\,\mu$H at 10 MHz, supplying an output power of 226.4 W. A DC-DC efficiency of 75.1% was recorded.

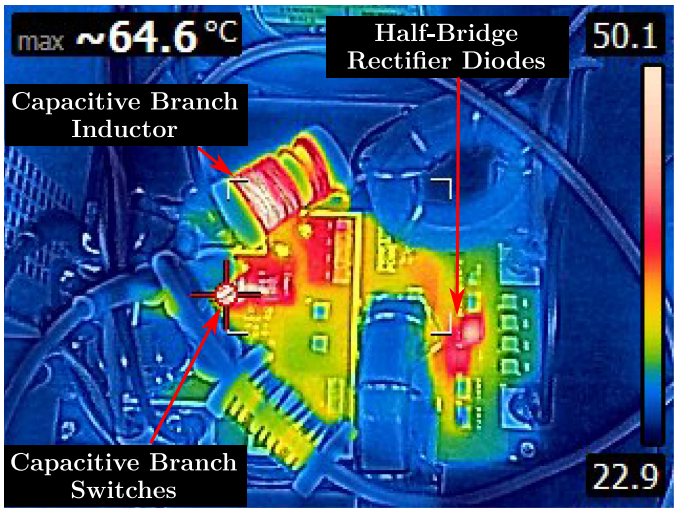

Fig. 28. Thermal image of the designed prototype operating at full load.

A phase shift of $\phi_{LC} = 164°$ was introduced between the two branches. The switches were again driven with square wave gate signals at 10 MHz with $D = 0.5$. The experimental results provided in Fig. 27 show that ZVS operation is exhibited by the switches of both the Class E inverters. A sinusoidal RF current of 4.02 A rms at 10 MHz flows through the output inductance L_{tx}, which signifies the ac output current of the power amplifier circuit. A resulting power of 226.4 W is delivered to R_{DC}, at an efficiency of 75.1%. The voltage across the dc resistance and output dc current were 184.1 V and 1.23 A, respectively. These results show that the designed circuit is able to supply in excess of 200 W of power to the load, while maintaining ZVS operation for the inverter switches and ensuring good operational efficiency. The thermal image of the designed prototype operating at full load is shown in Fig. 28. The hotspots are located at the switches, the inductor of the capacitive branch and the half-bridge rectifier

TABLE II
SYSTEM EFFICIENCY VERSUS OUTPUT POWER (FREQ. : 10 MHZ, D : 50%, ϕ_{LC} : 164°), R_{DC} : 150 Ω, L_{TX} : 2.33 μH

P_{out}	V_C, I_C	V_L , I_L	K_{LC}	P_{in}	η
25.1 W	12.2 V, 2.37 A	8.7 V, 0.93 A	0.71	36.9 W	68%
50.2 W	16.9 V, 3.31 A	11.6 V, 1.25 A	0.69	70.5 W	71.2%
75.4 W	20.1 V, 3.98 A	14.9 V, 1.56 A	0.74	103 W	73.2%
101.8 W	23.5 V, 4.53 A	17.4 V, 1.78 A	0.74	137.2 W	74.2%
125.9 W	25.9 V, 4.97 A	20 V, 1.98 A	0.77	168.4 W	74.8%
151.7 W	28.6 V, 5.41 A	21.8 V, 2.15 A	0.76	201.9 W	75.1%
176.7 W	30.9 V, 5.8 A	23.8 V, 2.3 A	0.77	234 W	75.5%
202.9 W	33.1 V, 6.13 A	26.5 V, 2.47 A	0.8	268.2 W	75.6%
226.4 W	35.5 V, 6.45 A	27.8 V, 2.6 A	0.78	301 W	75.1%

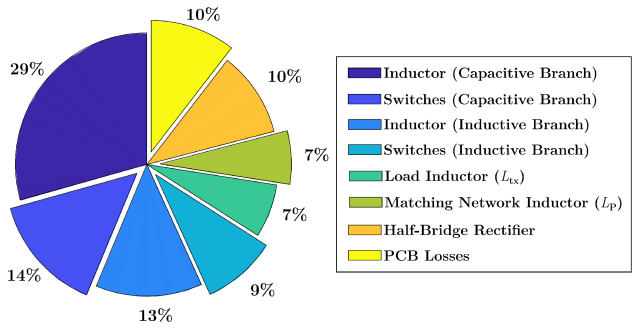

Fig. 29. Loss Analysis for the designed system when operating at full load.

diodes. The losses in the capacitive branch switches are mainly due to the C_{oss} losses in GaN devices at high voltage stresses at high frequencies [40], [41]. The wire-wound inductors suffer from large conduction losses, especially in the capacitive branch, which delivers bulk of the power to the output, resulting in larger currents in this branch. Since the half-bridge rectifier is made of SiC diodes, which are not designed to operate at high frequencies such as 10 MHz, as well as because these diodes are not actively cooled, these devices also get heated and contribute to the overall system losses. However, these diodes are effectively not part of the dc–ac inverter designed to drive an ICP reactor load. Thus, the dc–ac efficiency of the system is expected to be larger than the reported dc–dc efficiency value.

C. System Efficiency Measurement

The ICP driver circuit's efficiency was also measured at different output powers. For these measurements, the same output load as the previous test cases was used, that is $R_{DC} = 150\,\Omega$ and $L_{tx} = 2.33\,\mu$H. The phase shift ϕ_{LC} between the two Class E inverter branches was held constant at 164°. Slight adjustments were made to the input voltage ratio K_{LC} to ensure that the switches in both branches exhibit ZVS, thus allowing optimal operational efficiency at the considered output power. These efficiency values are tabulated in Table II. The efficiency values show a monotonical increase with output power, up to an output power of 202.9 W, where a peak efficiency of 75.6% is registered. In addition, the loss analysis of the designed system at full load is provided in Fig. 29. As discussed previously, the majority of the operational losses are due to the conduction losses through the inductors. At a frequency of 10 MHz, skin

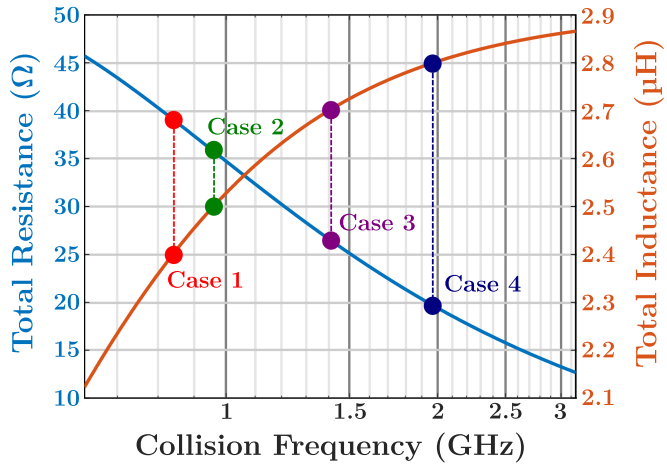

Fig. 30. Four load points on the impedance curve of the considered ICP reactor for which the designed power amplifier circuit's operation was tested.

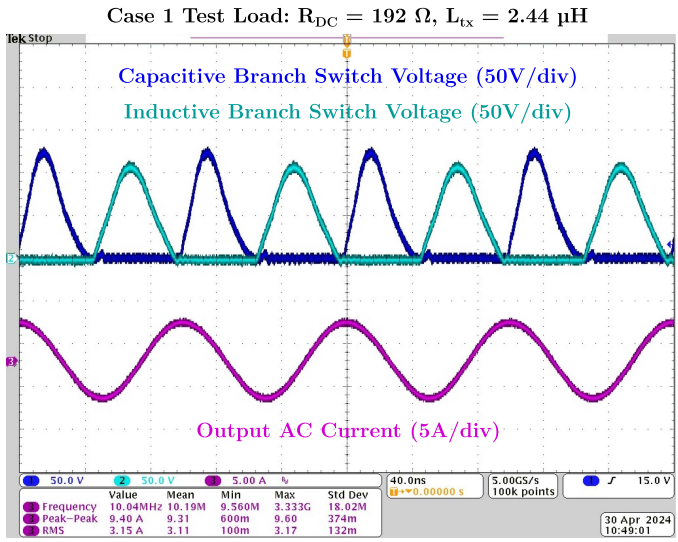

Fig. 31. Experimental results for Case 1: $K_{LC} = 1.03$ and $\phi_{LC} = 168°$. The load is $R_{DC} = 192\,\Omega$ and $L_{tx} = 2.44\,\mu$H at 10 MHz. The output DC power is 154.8 W with a DC-DC efficiency of 75.8% and ZVS operation.

effect greatly increases the resistance of the AWG-14 copper wires forming the windings of these inductors. Due to the use of the high frequency Fair-rite 67 core material, the core losses in the cored inductors (L_{tx} and L_P) are very small. Thus, the operational efficiency of the system can be improved by using high-Q HF inductors with low winding resistance, which would minimize the overall system conduction losses. Moreover, at higher output powers, the voltage stress across the switches during their off-state increases, as can be seen in Fig. 27. As a result, C_{oss} losses in GaN devices, as documented in [40] and [41], begin to become more dominant. Fig. 29 shows that despite ZVS, the GaN switches account for 23% of the total losses. This makes active cooling mandatory for GaN switches when operating them at high frequencies and high voltage stresses. The diodes of the output side half-bridge rectifier, as well as the PCB board conduction losses, also contribute significantly to the total system loss.

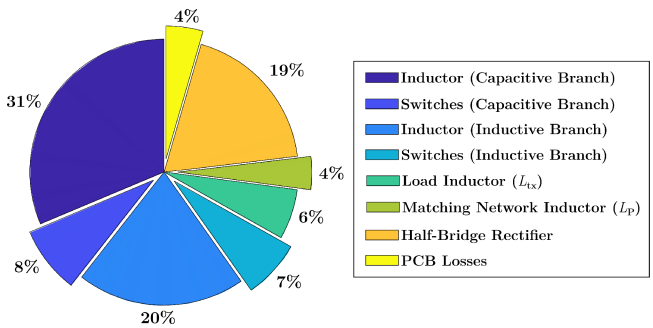

Fig. 32. Loss Analysis for Case 1 Test Load: $R_{DC} = 192\,\Omega$ and $L_{tx} = 2.44\,\mu$H at 10 MHz.

D. Performance Verification At Different Load Conditions

The proposed high frequency resonant power amplifier was designed with the purpose of being able to drive a variable impedance ICP reactor load without losing ZVS. Thus, the operation of the prototype was tested for different load points on the impedance curve of the considered ICP reactor, in addition to the load point considered in the previous experimental results. Four such load points were selected as shown in Fig. 30, which are 1) Case 1: $R_{tx} = 39\,\Omega$, $R_{DC} = 192\,\Omega$ and $L_{tx} = 2.4\,\mu$H; 2) Case 2: $R_{tx} = 36\,\Omega$, $R_{DC} = 178\,\Omega$ and $L_{tx} = 2.5\,\mu$H; 3) Case 3: $R_{tx} = 26\,\Omega$, $R_{DC} = 128\,\Omega$ and $L_{tx} = 2.7\,\mu$H; 4) Case 4: $R_{tx} = 20\,\Omega$, $R_{DC} = 100\,\Omega$ and $L_{tx} = 2.8\,\mu$H. For cases 1 and 2, a 2.44 μH toroidal inductor was used as the series load inductor, while for cases 3 and 4, a 2.75 μH toroidal inductor was used. Both these inductors used a Fair-rite 67 material core with 14 AWG enamelled copper wire windings.

1) *Case 1:* The input voltages and currents to the capacitive and inductive branch Class E inverters of the designed prototype are 27.13 V, 6.11 A and 27.94 V, 1.38 A, resulting in a K_{LC} of 1.03. The capacitive branch inverter provides more power to the load to compensate for the inductive nature of the effective load seen at the output terminal of the RSN. The phase shift ϕ_{LC} between the two inverters was set as 168°. The experimental results for this case, driving a load of $R_{DC} = 192\,\Omega$ and $L_{tx} = 2.44\,\mu$H are provided in Fig. 31. The switches in both branches operate in the ZVS mode, as desired, resulting in an output dc voltage and power of 172.4 V and 154.8 W, with an operational efficiency of 75.8%. The loss analysis for this operation case is provided in Fig. 32. The majority of the losses are accounted for by the conduction losses in the inductors, especially in the inductor of the capacitive branch. The half-bridge rectifier with SiC diodes is also responsible for a considerable amount of the total loss, leading to an estimated dc-ac efficiency of 80.4% for the designed system. Since the voltage stresses on the GaN devices are small, the C_{oss} losses are comparatively smaller for this case.

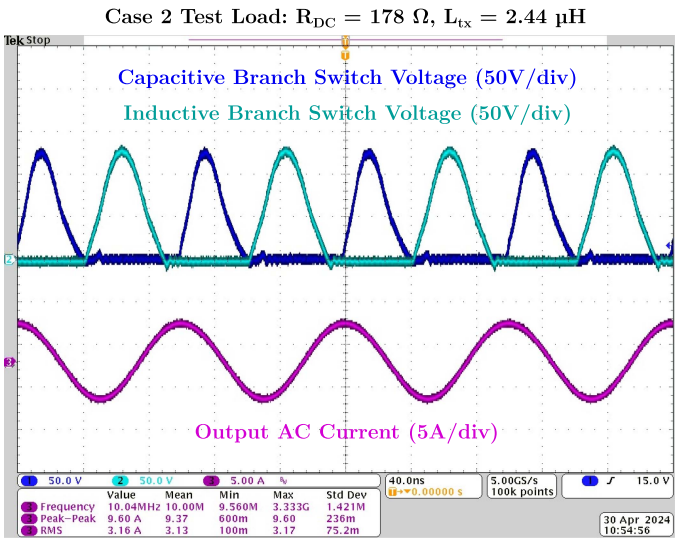

Fig. 33. Experimental results for Case 2: $K_{LC} = 1.2$ and $\phi_{LC} = 156°$. The load is $R_{DC} = 178\,\Omega$ and $L_{tx} = 2.44\,\mu$H at 10 MHz. The output DC power of 150.8 W. The DC-DC efficiency is 73.3% with ZVS operation.

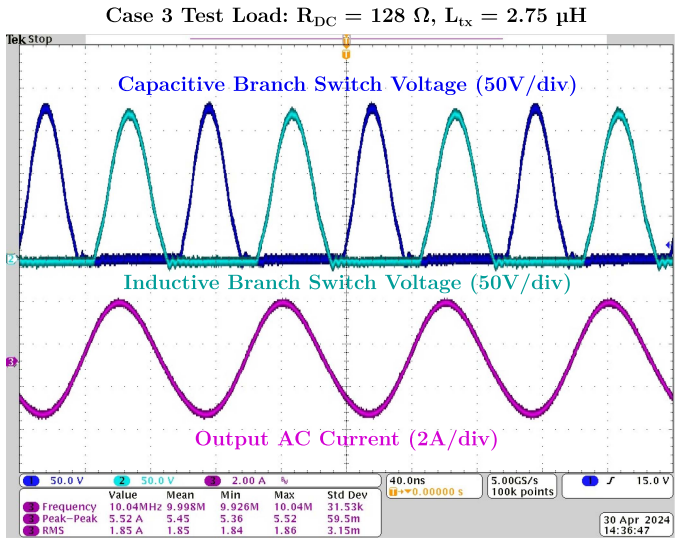

Fig. 35. Experimental results for Case 3: The driven load is $R_{DC} = 128\,\Omega$ and $L_{tx} = 2.75\,\mu$H at 10 MHz, supplying an output power of 38.4 W. K_{LC} and ϕ_{LC} are 1.14 and 166°, respectively. The measured efficiency for this case was 38.2% with ZVS operation.

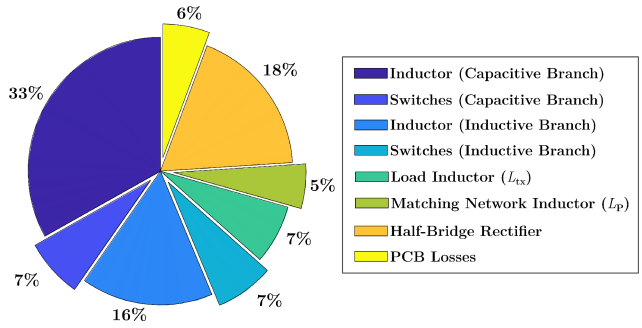

Fig. 34. Loss Analysis for Case 2 Test Load: $R_{DC} = 178\,\Omega$ and $L_{tx} = 2.44\,\mu$H at 10 MHz.

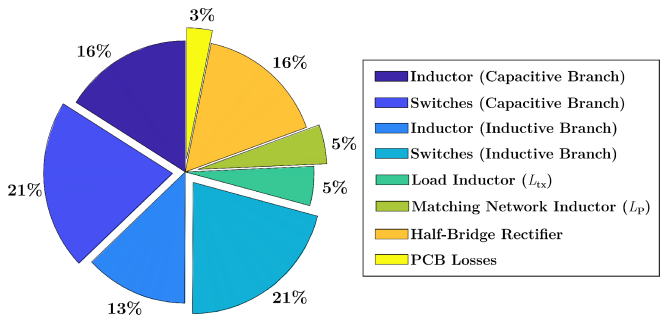

Fig. 36. Loss Analysis for Case 3 Test Load: $R_{DC} = 128\,\Omega$ and $L_{tx} = 2.75\,\mu$H at 10 MHz.

2) *Case 2:* The input voltages and currents to the capacitive and inductive branch Class E inverters of the designed prototype are 26.6 V, 6.59 A and 31.97 V, 0.95 A. Therefore, the K_{LC} is 1.2. The phase shift ϕ_{LC} is 156° and the capacitive branch delivers the bulk of the power. The experimental results for this case, when the designed prototype drives a load of $R_{DC} = 178\ \Omega$ and $L_{tx} = 2.44\,\mu$H are provided in Fig. 33. The switches in both branches operate in the ZVS mode. The output dc voltage and power are 163.9 V and 150.8 W, with an operational efficiency of 73.3%. Fig. 34 shows the loss analysis for this case. Due to a mode of operation similar to Case 1, the loss breakdown in Case 2 shows a similar pattern.
3) *Case 3:* The input voltages and currents to the capacitive and inductive branch Class E inverters of the designed prototype, when driving a load of $R_{DC} = 128\ \Omega$ and $L_{tx} = 2.75\,\mu$H are 38.58 V, 1.69 A and 43.98 V, 0.8 A. The K_{LC} is 1.14 and the phase shift ϕ_{LC} is 166°. The experimental results for this case are provided in Fig. 35. The switches in both branches operate in the ZVS mode. The resulting output dc voltage and power of 69.8 V and 38.4 W, with an operational efficiency of 38.2%. Since the power absorption efficiency of the plasma reduces with a decrease in the plasma resistance [30], this load case was tested at a low power level to emulate plasma behavior. The loss distribution for the system when driving this load is shown in Fig. 36. Due to the highly inductive nature of the load, the circulating currents within the system contribute to the HF conduction losses across the parasitic resistances of the magnetic components. Moreover, larger input voltages are required for providing a particular amount of power to such an output load, as the effective impedance seen at the output terminals of the Class-E inverters due to the RSN are larger for this case. Therefore, the voltage across the switches of the inverters during the off-state have larger peak values as well as a higher $\frac{dv}{dt}$ [41], which results in larger C_{oss} losses. This is evident from Fig. 36 where almost half of the total loss is attributed to the GaN devices. All these factors, together with the diode

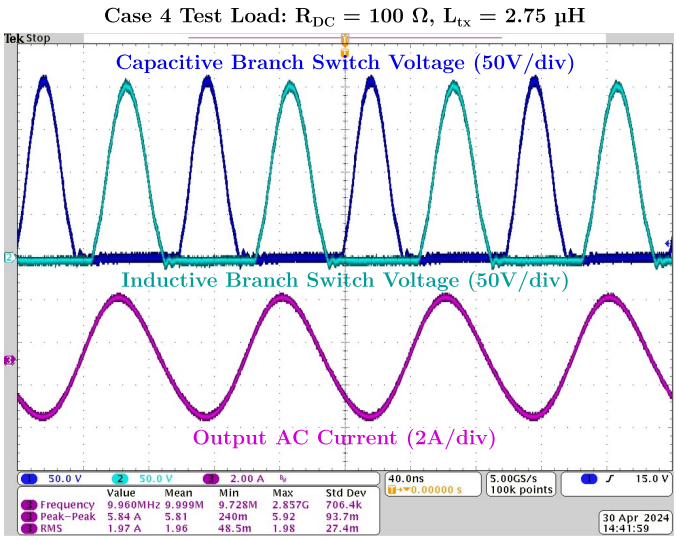

Fig. 37. Experimental results for Case 4: The driven load is $R_{\mathrm{DC}} = 100\,\Omega$ and $L_{\mathrm{tx}} = 2.75\,\mu$H at 10 MHz, supplying an output power of 36.24 W. The K_{LC} and ϕ_{LC} are 1.12 and 169°, respectively. The measured efficiency for this case was 35%, with ZVS operation.

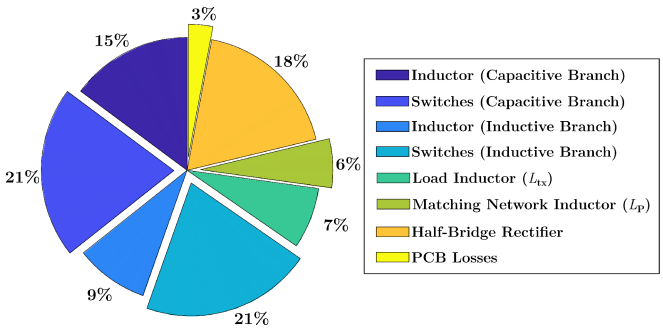

Fig. 38. Loss Analysis for Case 4 Test Load: $R_{\mathrm{DC}} = 100\,\Omega$ and $L_{\mathrm{tx}} = 2.75\,\mu$H at 10 MHz.

switching losses, negatively impact the efficiency of the prototype, even if the switches operate with ZVS.

4) *Case 4:* The input voltages and currents to the capacitive and inductive branch Class E inverters of the designed prototype, when driving a load of $R_{\mathrm{DC}} = 100\ \Omega$ and $L_{\mathrm{tx}} = 2.75\,\mu$H are 41.15 V, 1.68 A and 45.99 V, 0.75 A, resulting in a K_{LC} of 1.12. The phase shift ϕ_{LC} is set as 169°. The experimental results are shown in Fig. 37. As per the expected behavior, the switches in both branches operate in the ZVS mode. The output dc voltage and power of 60.4 V and 36.24 W, with an operational efficiency of 35%. This load is more inductive in nature, which explains the lower efficiency. Once again, the circuit efficiency suffers due to the increased C_{oss} losses encountered by the switches, despite ZVS operation, as well as higher conduction losses due to reactive power circulation and the diode switching losses. As a result, the loss distribution for this mode of operation, shown in Fig. 38 is similar to that for Case 3.

From these experimental results, it is evident that the designed high frequency resonant power amplifier prototype designed for driving a variable impedance ICP reactor load is indeed capable of maintaining ZVS over a wide load range and provide the desired performance. However, as the load impedance increases and becomes more inductive, as is the trend from Case 1 to Case 4 mentioned above, larger input voltages are required for providing the same amount of power to the load, with a greater amount of reactive power circulating within the system, leading to high HF conduction losses. Also, with larger input voltages, the voltage peaks of the off-state voltage across the switches of the Class E inverters increases. Since GaN devices are used as the switching devices, the C_{oss} losses increase considerably which greatly reduces the efficiency of the designed system, especially at low output power levels, even if the switches are operating with ZVS.

VI. Conclusion

This article presents the design and implementation of a radio frequency power combining system with reactance steering network for fusion plasma heating. This system was designed to drive variable impedance ICP reactor loads with RF currents to heat plasma through inductive discharge. A physics-based model of the ICP was used to estimate the variation in the load impedance. A matching network and an RSN converts the impedances seen at the output terminals of the Class E inverters to be mostly resistive to ensure ZVS. A prototype system was tested for different operating conditions with the load used for these tests emulating the behavior of an ICP reactor. It is capable of delivering powers in excess of 200 W at 10 MHz with the switches of both inverters operating with ZVS, thus ensuring a good operational dc–dc efficiency of around 75%, which takes into account the switching losses in the diodes of the output half-bridge rectifier. The prototype was also tested at a number of different load impedance values, taken from the impedance curve of the modeled ICP reactor, to verify that the proposed architecture is capable of operating with ZVS across a wide range of load impedances.

Appendix

A. Solenoidal ICP Modeling

ICP reactors can broadly be divided into two geometrical types, the planar coil and the solenoidal coil, as discussed previously. A diagrammatic representation of a solenoidal ICP reactor is provided in Fig. 39. The RF current carrying coils are wound in a helical manner around the plasma chamber, which is a hollow cylindrical chamber with an outer radius r_c and an inner radius r_o, surrounded by a dielectric wall of thickness $r_c - r_o$. When this coil is driven with large currents, the ICP operates in the H-mode with an electromagnetic field being induced in the plasma, which in turn drives an RF current in the plasma. This RF current inside the plasma has a skin depth of δ. The skin depth is dependent on the electron collision frequency or the electron pressure of the plasma and is usually much larger than the thickness of the dielectric sheath [30]. Thus, it can be seen that

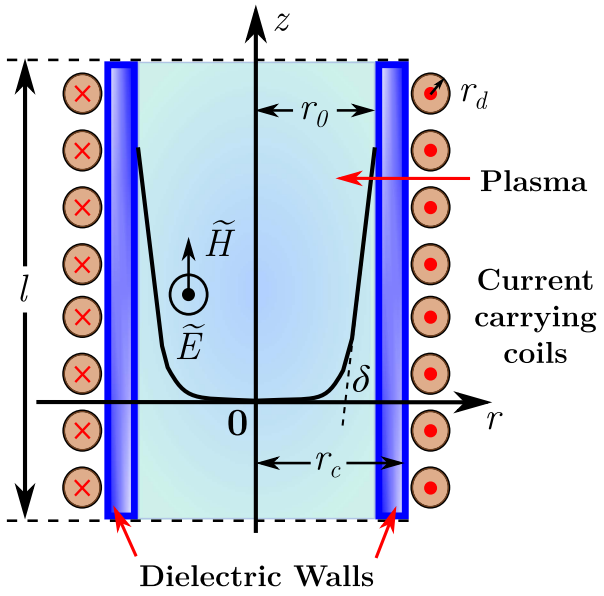

Fig. 39. 2-D cross section representation of the solenoidal ICP reactor, with the directions of the coil current and plasma current.

the mode of energy transfer in the plasma and its characteristics are greatly dependent on the plasma characteristics such as the plasma electron density n_e and the collision frequency ν_{m}.

Energy transfer through inductive discharges in the plasma can be modeled using the transformer model of the ICP. This transformer model is useful to develop the impedance model for the ICP. For the purpose of this article, we assume that the ICP load is driven in the H-mode with high RF currents, at high electron pressure or collision frequencies ($\nu_{\mathrm{m}} \gg \omega$), where ω is the angular frequency of the RF current in the coil, as well as high plasma electron densities. From the transformer model of the ICP shown in Fig. 7, the plasma resistance R_{p} is given by

$$R_{\mathrm{p}} = \frac{2\pi}{l\omega\epsilon_0}\mathrm{Re}\left[\frac{\mathrm{i}kr_0\mathrm{J}_1(kr_0)}{\epsilon_{\mathrm{p}}\mathrm{J}_0(kr_0)}\right] \tag{A.1}$$

where l and r_0 are the dimensions of the plasma chamber, shown in Fig. 39, and k is the complex wavenumber in the plasma [30], [42]. J_{n} is the Bessel function of the nth order. The relative plasma permittivity, ϵ_{p}, is a complex number and is a function of the electron density n_{e}, the collision frequency ν_{m} and the mass of an electron m_{e}

$$\epsilon_{\mathrm{p}} = 1 - \frac{n_{\mathrm{e}}e^2}{m_{\mathrm{e}}\epsilon_0}\frac{1}{\omega(\omega - i\nu_{\mathrm{m}})}. \tag{A.2}$$

The plasma inductance L_{P} is attributed in part to the electron inertia. This inertial plasma inductance, L_{p}, can be expressed as a function of the plasma resistance R_{p} and ν_{m} as

$$L_{\mathrm{p}} = \frac{R_{\mathrm{p}}}{\nu_{\mathrm{m}}} = \frac{2\pi}{\nu_{\mathrm{m}}l\omega\epsilon_0}\mathrm{Re}\left[\frac{\mathrm{i}kr_0\mathrm{J}_1(kr_0)}{\epsilon_{\mathrm{p}}\mathrm{J}_0(kr_0)}\right]. \tag{A.3}$$

On the other hand, the coupling inductance L_{mp}, which couples the current in the external coil to the plasma, and which forms the second part of the plasma inductance, can be estimated by the following relation [30]

$$L_{\mathrm{mp}} = \frac{\mu_0\pi {r_0}^2}{l}. \tag{A.4}$$

The lumped transformer model resistance R_{s} and inductance L_{s} of the ICP can computed by

$$R_{\mathrm{s}} = R_{\mathrm{coil}} + N^2R_{\mathrm{p}} \tag{A.5}$$

$$L_{\mathrm{s}} = L_{\mathrm{coil}} - N^2(L_{\mathrm{mp}} + L_{\mathrm{p}}). \tag{A.6}$$

Using these equations, the impedance of the ICP can be estimated according to varying plasma characteristics, such as plasma electron density n_{e} and the electron collision frequency ν_{m}. These variations have been calculated according to standard values of n_{e} and ν_{m}, and have been presented in Section III.

B. Matching Network Calculations

Since the reference load impedance Z_{ref} based on which the LC matching network is designed is also a series inductive load, it can also be decomposed into its resistive and reactive part

$$Z_{\mathrm{ref}} = R_{\mathrm{tx}} + jX_{\mathrm{tx}}. \tag{A.7}$$

This reference series inductive ICP load is then converted into its equivalent parallel configuration, as shown in Fig. 12 [43]. The resistance and reactance values (R_{txp} and X_{txp}) of the parallel configuration of the load are calculated as follows:

$$Q_{\mathrm{SL}} = Q_{\mathrm{PL}} = \frac{X_{\mathrm{tx}}}{R_{\mathrm{tx}}}. \tag{A.8}$$

$$R_{\mathrm{txp}} = R_{\mathrm{tx}}(Q_{\mathrm{PL}}^2 + 1). \tag{A.9}$$

$$X_{\mathrm{txp}} = \frac{R_{\mathrm{txp}}}{Q_{\mathrm{PL}}}. \tag{A.10}$$

Here, Q_{SL} and Q_{PL} denote the series and parallel quality factor of the load, which are taken to be equal. The values of R_{txp} and X_{txp} are calculated from R_{tx} and X_{tx} according to (A.9) and (A.10), respectively. This reactive part of the parallel load is then absorbed into the matching network during the design process, which converts the load to be matched to be purely resistive. Then, a suitable source impedance R_{S} is selected to which the equivalent parallel resistance R_{txp} of the reference ICP load impedance is matched. A lower value of the source impedance allows for larger impedance compression and a larger Q-factor (Q_{S} and Q_{P}) for the matching network

$$Q_{\mathrm{S}} = Q_{\mathrm{P}} = \sqrt{\frac{R_{\mathrm{txp}}}{R_{\mathrm{S}}} - 1}. \tag{A.11}$$

Using the Q-factor, the component values for the single-stage matching network, L_{P} and C_{S}, shown in Fig. 12, can be determined according to the following equations:

$$L_{\mathrm{P}} = \frac{R_{\mathrm{txp}}}{2\pi f_{\mathrm{S}}(Q_{\mathrm{P}} - Q_{\mathrm{PL}})}. \tag{A.12}$$

$$C_{\mathrm{S}} = \frac{1}{2\pi f_s Q_{\mathrm{S}} R_{\mathrm{S}}}. \tag{A.13}$$

In these equations, f_{S} refers to the nominal frequency for which the matching network is designed. We find that for larger

Q-values, the value of L_P gets smaller. Since the size of the matching network is dominated by the magnetic component L_P, a lower value of R_S also helps reduce the size of the matching network. A larger compression of the ICP load also allows the component values of the RSN to be smaller, allowing for an overall more compact design. However, for smaller R_S, the cut-off frequency of the matching network increases. Depending on the frequency of operation of the system, a lower bound can be set on the value of R_S. Candidate matching network designs are computed for this range of R_S values. Finally, the R_S value is selected which provides the best design in terms of impedance compression and cut-off frequency, and that satisfies the design constraints for the RSN.

REFERENCES

[1] T. Sen, M. Liao, Y. Elasser, and M. Chen, "Power amplifiers with reactance steering network for efficient driving of variable impedance inductively coupled plasma coils," in *Proc. IEEE Appl. Power Electron. Conf. Expo.*, 2024, pp. 2136–2143.

[2] N. Peacock, D. Robinson, M. Forrest, P. D. Wilcock, and V. V. Sannikov, "Measurement of the electron temperature by Thomson scattering in Tokamak T3," *Nature*, vol. 224, pp. 488–490, 1969.

[3] ITER Newsline, "Neutral beam: The system that makes the tokamak feel small," [Online]. Available: ter.org/newsline/-/3254

[4] S. J. Wukitch, "Plasma heating & current drive," [Online]. Available: https://www.psfc.mit.edu/research/topics/plasma-heating-current-drive

[5] E. T. Supra, "Theory and experiments on R.F. plasma heating, current drive and profile control in tore supra," *Fusion Eng. Des.*, vol. 26, no. 1, pp. 29–48, 1995.

[6] R. Dumont, "Magnetic confinement fusion - plasma theory: Heating and current drive," in *Encyclopedia of Nuclear Energy*, Elsevier, 2021. [Online]. Available: https://cea.hal.science/cea-03134128

[7] T. Ueda, "Reliability issues in GAN and sic power devices," in *Proc. IEEE Int. Rel. Phys. Symp.*, 2014, pp. 3D.4.1–3D.4.6.

[8] A. Bhalla, "Practical considerations when comparing SiC and GaN in power applications," 2018. [Online]. Available: https://www.qorvo.com/resources/d/practical-considerations-when-comparing-sic-and-gan-in-power-applications-white-paper

[9] N. Sokal, "Class e high-efficiency switching-mode tuned power amplifier with only one inductor and one capacitor in load network-approximate analysis," *IEEE J. Solid-State Circuits*, vol. 16, no. 4, pp. 380–384, Aug. 1981.

[10] J. M. Rivas, Y. Han, O. Leitermann, A. Sagneri, and D. J. Perreault, "A high-frequency resonant inverter topology with low voltage stress," in *Proc. 2007 IEEE Power Electron. Specialists Conf.*, 2007, pp. 2705–2717.

[11] Y. Han, O. Leitermann, D. A. Jackson, J. M. Rivas, and D. J. Perreault, "Resistance compression networks for radio-frequency power conversion," *IEEE Trans. Power Electron.*, vol. 22, no. 1, pp. 41–53, Jan. 2007.

[12] W. D. Braun and D. J. Perreault, "A high-frequency inverter for variable-load operation," *IEEE Trans. Emerg. Sel. Topics Power Electron.*, vol. 7, no. 2, pp. 706–721, Jul. 2019.

[13] L. Roslaniec, A. S. Jurkov, A. A. Bastami, and D. J. Perreault, "Design of single-switch inverters for variable resistance/load modulation operation," *IEEE Trans. Power Electron.*, vol. 30, no. 6, pp. 3200–3214, Jun. 2015.

[14] P. A. Godoy, D. J. Perreault, and J. L. Dawson, "Outphasing energy recovery amplifier with resistance compression for improved efficiency," *IEEE Trans. Microw. Theory Techn.*, vol. 57, no. 12, pp. 2895–2906, Dec. 2009.

[15] H. Zhang, G. Cassidy, A. Jurkov, K. Luu, A. Radomski, and D. J. Perreault, "A high-power non-isolating RF power combining network based on transmission lines," *IEEE J. Emerg. Sel. Topics Ind. Electron.*, vol. 5, no. 3, pp. 1006–1016, Jul. 2024.

[16] T. W. Barton, A. S. Jurkov, P. H. Pednekar, and D. J. Perreault, "Multi-way lossless outphasing system based on an all-transmission-line combiner," *IEEE Trans. Microw. Theory Techn.*, vol. 64, no. 4, pp. 1313–1326, Apr. 2016.

[17] D. J. Perreault, "A new power combining and outphasing modulation system for high-efficiency power amplification," *IEEE Trans. Circuits Syst. I: Reg. Papers*, vol. 58, no. 8, pp. 1713–1726, Aug. 2011.

[18] J.-S. Fu and A. Mortazawi, "Improving power amplifier efficiency and linearity using a dynamically controlled tunable matching network," *IEEE Trans. Microw. Theory Techn.*, vol. 56, no. 12, pp. 3239–3244, Dec. 2008.

[19] C. Hoarau, N. Corrao, J.-D. Arnould, P. Ferrari, and P. Xavier, "Complete design and measurement methodology for a tunable RF impedance-matching network," *IEEE Trans. Microw. Theory Techn.*, vol. 56, no. 11, pp. 2620–2627, Nov. 2008.

[20] Y. Yoon et al., "A dual-mode CMOS RF power amplifier with integrated tunable matching network," *IEEE Trans. Microw. Theory Techn.*, vol. 60, no. 1, pp. 77–88, Jan. 2012.

[21] A. S. Jurkov, A. Radomski, and D. J. Perreault, "Tunable matching networks based on phase-switched impedance modulation," *IEEE Trans. Power Electron.*, vol. 35, no. 10, pp. 10150–10167, Oct. 2020.

[22] A. Al Bastami et al., "Dynamic matching system for radio-frequency plasma generation," *IEEE Trans. Power Electron.*, vol. 33, no. 3, pp. 1940–1951, Mar. 2018.

[23] N. Kumar, C. Prakash, A. Grebennikov, and A. Mediano, "High-efficiency broadband parallel-circuit class E RF power amplifier with reactance-compensation technique," *IEEE Trans. Microw. Theory Techn.*, vol. 56, no. 3, pp. 604–612, Mar. 2008.

[24] J. Xu, K. Surakitbovorn, B. Wang, M. A. Cappelli, and J. Rivas-Davila, "Frequency-selective mhz power amplifier for dielectric barrier discharge plasma generation," *IEEE Open J. Power Electron.*, vol. 3, pp. 846–855, 2022.

[25] G. McCracken and P. Stott, *Fusion the Energy of the Universe*. New York, NY, USA: Academic Press, 2012.

[26] G. S. Nusinovich, M. K. A. Thumm, and M. I. Petelin, "The gyrotron at 50: Historical overview," *J. Infrared, Millimeter, Terahertz Waves*, vol. 35, pp. 325–381, 2014.

[27] M. Hruszowiec, W. Czarczyński, E. F. Pliński, and T. Wickowski, "Gyrotron technology," *J. Telecommun. Inf. Technol.*, pp. 68–76, Mar. 2014.

[28] R. Kramen, "Heating for fusion: Why toast plasma when you can microwave it," [Online]. Available: https://www.pppl.gov/news/2024/heating-fusion-why-toast-plasma-when-you-can-microwave-it

[29] M.-H. Lee and C.-W. Chung, "On the E to H and H to E transition mechanisms in inductively coupled plasma," *Phys. Plasmas*, vol. 13, no. 6, 2006, Art. no. 063510.

[30] P. Chabert and N. Braithwaite, *Physics of Radio-Frequency Plasmas*. Cambridge, U.K.: Cambridge Univ. Press, 2011.

[31] K. Nishida et al., "Equivalent circuit of radio frequency-plasma with the transformer model," *Rev. Sci. Instrum.*, vol. 85, no. 2, 2013, Art. no. 02B117.

[32] I. M. El-Fayoumi and I. R. Jones, "The electromagnetic basis of the transformer model for an inductively coupled RF plasma source," *Plasma Sources Sci. Technol.*, vol. 7, no. 2, 1998, Art. no. 179, doi: 10.1088/0963-0252/7/2/012.

[33] J. J. Lee, S. J. Kim, K. K. Kim, Y. S. Lee, and S. J. You, "A simple model of solenoidal inductively coupled plasma sources considering finite size," *AIP Adv.*, vol. 10, no. 3, 2020, Art. no. 035008, doi: 10.1063/1.5133862.

[34] P. Colpo, R. Ernst, and F. Rossi, "Determination of the equivalent circuit of inductively coupled plasma sources," *J. Appl. Phys.*, vol. 85, no. 3, pp. 1366–1371, 1999.

[35] L. J. Mahoney, A. E. Wendt, E. Barrios, C. J. Richards, and J. L. Shohet, "Electron-density and energy distributions in a planar inductively coupled discharge," *J. Appl. Phys.*, vol. 76, no. 4, pp. 2041–2047, 1994, doi: 10.1063/1.357672.

[36] H.-C. Lee, "Review of inductively coupled plasmas: Nano-applications and bistable hysteresis physics," *Appl. Phys. Rev.*, vol. 5, no. 1, 2018, Art. no. 011108, doi: 10.1063/1.5012001.

[37] M. Liu and M. Chen, "Dual-band wireless power transfer with reactance steering network and reconfigurable receivers," *IEEE Trans. Power Electron.*, vol. 35, no. 1, pp. 496–507, Jan. 2020.

[38] I. Hakala, D. Choi, L. Gharavi, N. Kajakine, J. Koskela, and R. Kaunisto, "A 2.14-ghz chireix outphasing transmitter," *IEEE Trans. Microw. Theory Techn.*, vol. 53, no. 6, pp. 2129–2138, Jun. 2005.

[39] T.-P. Hung, D. K. Choi, L. E. Larson, and P. M. Asbeck, "CMOS outphasing class-d amplifier with chireix combiner," *IEEE Microw. Wireless Compon. Lett.*, vol. 17, no. 8, pp. 619–621, Aug. 2007.

[40] Q. Song, R. Zhang, Q. Li, and Y. Zhang, "Output capacitance loss of gan hemts in steady-state switching," *IEEE Trans. Power Electron.*, vol. 39, no. 5, pp. 5547–5557, May 2024.

[41] G. Zulauf, S. Park, W. Liang, K. N. Surakitbovorn, and J. Rivas-Davila, "Coss losses in 600 V GAN power semiconductors in soft-switched, high- and very-high-frequency power converters," *IEEE Trans. Power Electron.*, vol. 33, no. 12, pp. 10748–10763, Dec. 2018.

[42] W. Kobayashi, K. Nishida, S. Mattei, J. Lettry, and A. Hatayama, "Plasma impedance prediction model and impedance matching by frequency tuning in radio frequency negative ion sources," *AIP Conf. Proc.*, vol. 2011, no. 1, 09 2018, Art. no. 050019.
[43] *AN1275: Impedance Matching Network Architectures*. Silicon Laboratories Inc.

Tanuj Sen (Student Member, IEEE) received the bachelor's degree in electrical and electronics engineering from Birla Institute of Technology and Science, Pilani, India, in 2015, and the Master of Sciences degree in electrical engineering and information technology from ETH Zurich, Zurich, Switzerland, in 2019, respectively, and the M.A. degree in electrical and computer engineering, in 2022, from Princeton University, NJ, USA, where he is currently working toward the Ph.D. degree in electrical and computer engineering.

His research interests include the design of high-power density, high-frequency grid-connected and resonant power electronic inverters for powering plasma heating coils in fusion reactors, as well as the design and analysis of coupled inductors and their application in high-frequency power electronic circuits. He is also the recipient of the best technical presentation award and the best dialog presentation award at the IEEE Applied Power Electronics Conference 2023 and IEEE Applied Power Electronics Conference 2024, respectively.

Mian Liao (Student Member, IEEE) received the B.S. degree in electrical engineering from Virginia Tech, VA, USA, in 2020, and the M.A. degree in electrical engineering, in 2022, from Princeton University, NJ, USA, where he is currently working toward the Ph.D. degree in electrical and computer engineering.

His research interests include machine learning control in power electronics, point-of-load converters for data center applications, wireless power transfer for UAV applications, and grid-tied three-phase inverters.

Mr. Liao was the recipient of Fralin Undergraduate Research Fellowship (2019) while at Virginia Tech, New Jersey Economic Development Authority Wind Institute Fellowship (2023) while at Princeton University, Rao R. Tummala Best Paper Award and First Prize Presentation Award at 3D-PEIM (2023), and the Best Presentation Award in the 2024 IEEE APEC.

Youssef Elasser (Student Member, IEEE) received the B.S. degree in electrical engineering and computer science with a concentration in electric power from Rensselaer Polytechnic Institute, Troy, NY, USA, in 2018, and the Ph.D. degree in electrical and computer engineering from Princeton University, Princeton, NJ, USA, in 2024.

He is currently working as a Research Scientist with NVIDIA. His research interests include dc–dc power conversion, magnetics design, and optimization.

Dr. Elasser was the recipient of the Grainger Scholars Award for distinguished undergraduates studying electric power while at Rensselaer Polytechnic Institute (2018), two IEEE Transactions on Power Electronics Prize Paper Awards (2020, 2022), the first place award for the IEEE Energy Conversion Congress and Exposition Student Demonstration (2021), and the prestigious National Science Foundation Graduate Research Fellowship while at Princeton University.

Minjie Chen (Senior Member, IEEE) received the B.S. degree in electrical engineering from Tsinghua University, Beijing, China, in 2009, and the S.M., E.E., and Ph.D. degrees in electrical engineering and computer science from the Massachusetts Institute of Technology, Cambridge, MA, USA, in 2015.

He is an Assistant Professor of electrical and computer engineering and the Andlinger Center for Energy and the Environment with Princeton University, NJ, USA. His research interests include modeling, design, and application of high-performance power electronics.

Dr. Chen is a recipient of the IEEE PELS Richard M. Bass Outstanding Young Power Electronics Engineer Award, the Princeton SEAS E. Lawrence Keyes, Jr./Emerson Electric Co. Junior Faculty Award, the NSF CAREER Award, six IEEE Transactions on Power Electronics Prize Paper Awards, the MIT EECS D. N. Chorafas Ph.D. Thesis Award, and numerous conference paper awards from COMPEL, ICRA, IROS, ECCE, APEC, 3D-PEIM, and OCP. He was listed on the Princeton Engineering Commendation List for Outstanding Teaching multiple times.